

Visualizing interfacial collective reaction behaviour of Li–S batteries

<https://doi.org/10.1038/s41586-023-06326-8>

Received: 10 October 2022

Accepted: 14 June 2023

Published online: 6 September 2023

 Check for updates

Shiyuan Zhou^{1,8}, Jie Shi^{2,8}, Sangui Liu¹, Gen Li¹, Fei Pei¹, Youhu Chen¹, Junxian Deng¹, Qizheng Zheng¹, Jiayi Li³, Chen Zhao⁴, Inhui Hwang⁵, Cheng-Jun Sun⁵, Yuzi Liu⁶, Yu Deng³, Ling Huang¹, Yu Qiao^{1,7}, Gui-Liang Xu^{4,✉}, Jian-Feng Chen², Khalil Amine^{4,✉}, Shi-Gang Sun¹ & Hong-Gang Liao^{1,7,✉}

Benefiting from high energy density (2,600 Wh kg⁻¹) and low cost, lithium–sulfur (Li–S) batteries are considered promising candidates for advanced energy-storage systems^{1–4}. Despite tremendous efforts in suppressing the long-standing shuttle effect of lithium polysulfides^{5–7}, understanding of the interfacial reactions of lithium polysulfides at the nanoscale remains elusive. This is mainly because of the limitations of in situ characterization tools in tracing the liquid–solid conversion of unstable lithium polysulfides at high temporal–spatial resolution^{8–10}. There is an urgent need to understand the coupled phenomena inside Li–S batteries, specifically, the dynamic distribution, aggregation, deposition and dissolution of lithium polysulfides. Here, by using in situ liquid-cell electrochemical transmission electron microscopy, we directly visualized the transformation of lithium polysulfides over electrode surfaces at the atomic scale. Notably, an unexpected gathering-induced collective charge transfer of lithium polysulfides was captured on the nanocluster active-centre-immobilized surface. It further induced an instantaneous deposition of nonequilibrium Li₂S nanocrystals from the dense liquid phase of lithium polysulfides. Without mediation of active centres, the reactions followed a classical single-molecule pathway, lithium polysulfides transforming into Li₂S₂ and Li₂S step by step. Molecular dynamics simulations indicated that the long-range electrostatic interaction between active centres and lithium polysulfides promoted the formation of a dense phase consisting of Li⁺ and S_n²⁻ (2 < n ≤ 6), and the collective charge transfer in the dense phase was further verified by ab initio molecular dynamics simulations. The collective interfacial reaction pathway unveils a new transformation mechanism and deepens the fundamental understanding of Li–S batteries.

Lithium–sulfur (Li–S) batteries undergo a 16-electron reaction that converts sulfur into a series of lithium polysulfides (LiPSs) with variable chain length. Among them, three-quarters of the capacity is mainly contributed by the reaction from soluble Li₂S₆ to solid Li₂S (Fig. 1a). During this process, the high solubility of LiPSs species and insulating properties of Li₂S₂/Li₂S would lead to continuous loss of active materials and severe capacity degradation¹¹. Many strategies have been proposed to increase the energy density and cycling stability, such as structural tailoring of sulfur hosts¹², separators¹³, electrolytes¹⁴ etc. However, the fundamental principles underlying these material designs remain poorly understood. For example, what is the rate-limiting step of sluggish reaction kinetics that prevents development of fast-charging Li–S batteries? How does active centre remain active to catalyse LiPSs at electrode–electrolyte interfaces?

To study the electrochemical reactions of Li–S batteries, in situ characterization techniques, including X-ray diffraction (XRD)¹⁵, X-ray absorption near edge structure (XANES)^{16,17}, nuclear magnetic resonance¹⁸ and Raman spectra¹⁹, are used. These techniques can provide specific chemical/structural information of reaction intermediates/products; however, they mainly acquire statistical information of mixed signals from both electrolyte and electrode, resulting in the limited understanding of interfacial reaction dynamics of LiPSs. Benefiting from the high temporal–spatial resolution, in situ transmission electron microscopy (TEM) can track dynamic reactions at the atomic/single-molecule scale^{20,21}. At present, the open-cell configuration can barely avoid the spontaneous sublimation of sulfur under a high-vacuum environment^{22,23} and the previously reported liquid-cell configuration is driven by an electron beam (e-beam) instead

¹State Key Laboratory of Physical Chemistry of Solid Surfaces, Collaborative Innovation Center of Chemistry for Energy Materials, College of Chemistry and Chemical Engineering, Xiamen University, Xiamen, People's Republic of China. ²State Key Laboratory of Organic-Inorganic Composites, Beijing University of Chemical Technology, Beijing, People's Republic of China.

³Department of Materials Science and Engineering, College of Engineering and Applied Sciences, Nanjing University, Nanjing, People's Republic of China. ⁴Chemical Sciences and Engineering Division, Argonne National Laboratory, Lemont, IL, USA. ⁵X-ray Science Division, Argonne National Laboratory, Lemont, IL, USA. ⁶Center for Nanoscale Materials, Argonne National Laboratory, Lemont, IL, USA. ⁷Innovation Laboratory for Sciences and Technologies of Energy Materials of Fujian Province (IKKEM), Xiamen, People's Republic of China. ⁸These authors contributed equally: Shiyuan Zhou, Jie Shi. [✉]e-mail: xug@anl.gov; amine@anl.gov; hgliao@xmu.edu.cn

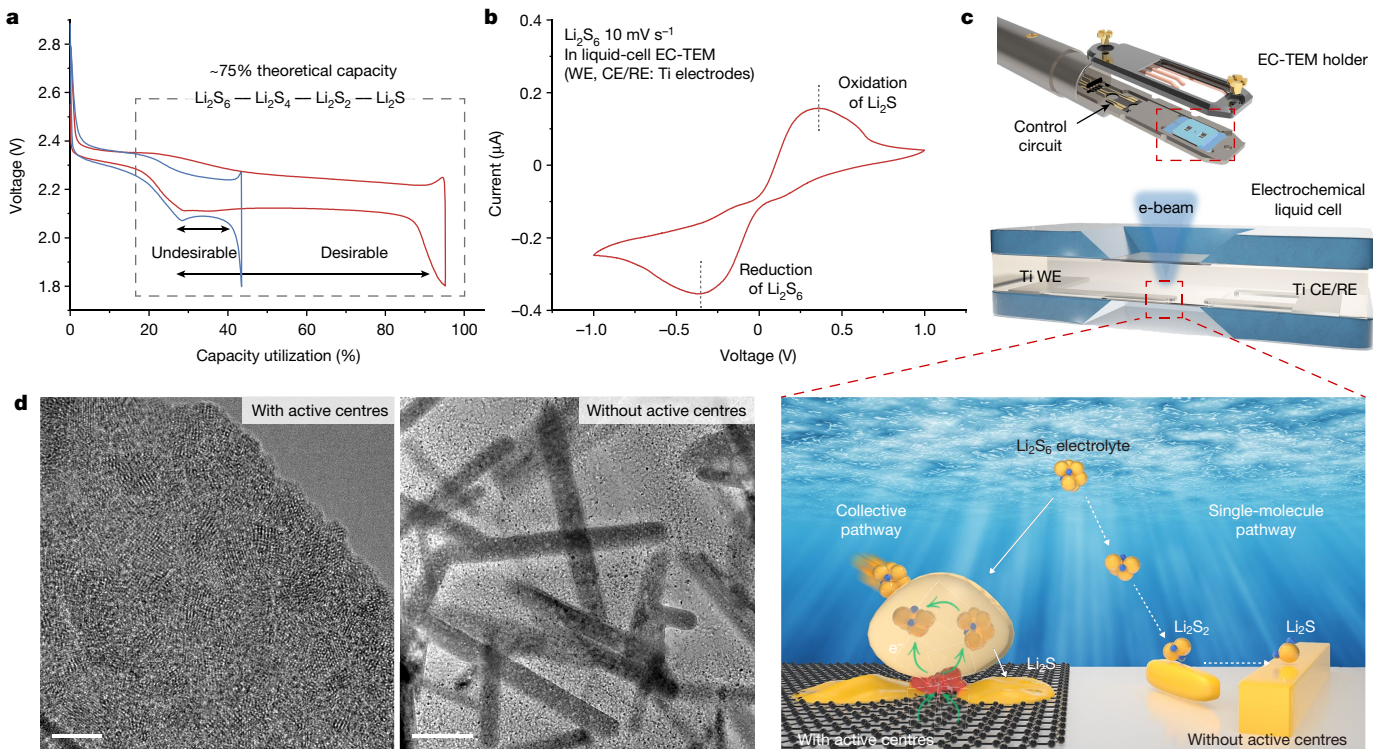


Fig. 1 | Design of liquid-cell EC-TEM to investigate the interfacial reactions of LiPSs. **a**, Comparison of charge–discharge profiles of desirable and undesirable Li_2S_6 – Li_2S reactions in Li–S batteries. **b**, CV profile obtained in an electrochemical liquid cell at a scan rate of 10 mV s^{-1} showing the reduction of Li_2S_6 and oxidation of Li_2S . **c**, Configuration of liquid-cell EC-TEM and schematic illustration of electrochemical reactions of LiPSs at different electrode–electrolyte interfaces. **d**, Typical (HR)TEM images of deposited Li_2S at different electrode surfaces (with (scale bar, 5 nm) and without (scale bar, 500 nm) active centres) after potentiostatic discharge at -0.5 V for 300 s in an electrochemical liquid cell. $10 \text{ mM Li}_2\text{S}_6$ was used as the electrolyte. CE/RE, counter/reference electrodes; WE, working electrode.

of an electric field^{24,25}, suffering from the unavoidable susceptibility to beam damage during investigation. The aforementioned in situ TEM studies have not yet uncovered the realistic electrochemical redox reactions in liquid electrolytes.

Here we constructed a Li–S nanobattery within a liquid cell, and combined with electrochemical transmission electron microscopy (EC-TEM), we achieved high-resolution and real-time observation of the evolution of LiPSs at electrode surfaces in an ether-based electrolyte (Fig. 1b–d). Our study showed that active centres gathered soluble LiPSs into a droplet-like dense phase and induced an instantaneous deposition of nonequilibrium nanocrystalline/amorphous Li_2S , rather than a traditional step-by-step transformation. Density functional theory (DFT) calculations and molecular dynamics (MD) simulations pointed out that gathering-induced crystallization resulted from the long-range electrostatic interaction and collective charge transfer behaviour between active centres and the droplet-like dense phase of LiPSs.

Configurations of EC-TEM

An electrochemical liquid cell using Ti as electrodes was assembled for Li_2S_6 electrolyte injection, before being mounted in an EC-TEM holder (Fig. 1c, Extended Data Fig. 1a–d and Supplementary Fig. 1). To enhance the spatial resolution in liquid cells, we applied a 100-nm-thick spacer and an approximately 10-nm SiN_x observation window (for more details of instrumental advancements, see Supplementary Discussion 1, Extended Data Fig. 1e,f and Supplementary Figs. 2–4). The cyclic voltammetry (CV) profile acquired in an electrochemical liquid cell reflected a pair of redox peaks (Fig. 1b), corresponding to the typical liquid–solid transformation of LiPSs. The liquid cell was potentiostatically discharged at -0.5 V for the deposition of Li_2S from soluble Li_2S_n

($\text{Li}_2\text{S}_n + \text{e}^- \rightarrow \text{Li}_2\text{S}, 2 < n \leq 6$). TEM images showed two distinct forms of deposited Li_2S —ultrasmall nanocrystalline (with active centres) and rod-like/plate-like structures (without active centres)—indicating a strong correlation between electrode surfaces and the thermodynamics/kinetics of Li_2S deposition (Fig. 1d).

Single-molecule pathway

High-resolution in situ EC-TEM studies were conducted to investigate electrochemical reactions at different electrode surfaces. Because LiPSs intermediates and pure Li_2S were highly susceptible to e-beam damage, all electrochemical processes in liquid cells were conducted with e-beam dose rates below $1.5 \text{ e } \text{\AA}^{-2} \text{ s}^{-1}$ (for more details of e-beam effects, see Supplementary Discussion 2 and Supplementary Figs. 5–10). Time-series TEM images and projection-area variation revealed the morphology evolution of Li_2S deposition/dissolution without mediation of active centres (Fig. 2a,b and Supplementary Video 1). During potentiostatic discharge at -0.5 V , two types of nucleation-growth pathway were observed: one was a single-step deposition of rod-like/plate-like Li_2S and the other was a two-step deposition by means of metastable Li_2S_2 . For the two-step pathway, solid nano-nuclei were formed at the electrode–electrolyte interface during initial nucleation (marked as particles 1 and 2 in Fig. 2b), which acted as preferred seeds for the subsequent grain growth (25 s). After about 70 s of discharge, the growth rate of primary Li_2S particles slowed down. Then, metastable particle 2 (smaller size) quickly dissolved, whereas particle 1 (larger size) elongated along its longitudinal orientation (116.2 s). After the complete dissolution of particle 2 and mass redistribution, rod-like Li_2S was formed (137.6 s). During potentiostatic charge ($+0.5 \text{ V}$), rod-like Li_2S shortened gradually (201.6 s) and then decomposed rapidly (219.8 s). The variation in dissolution rate (before/after about 240 s) should be

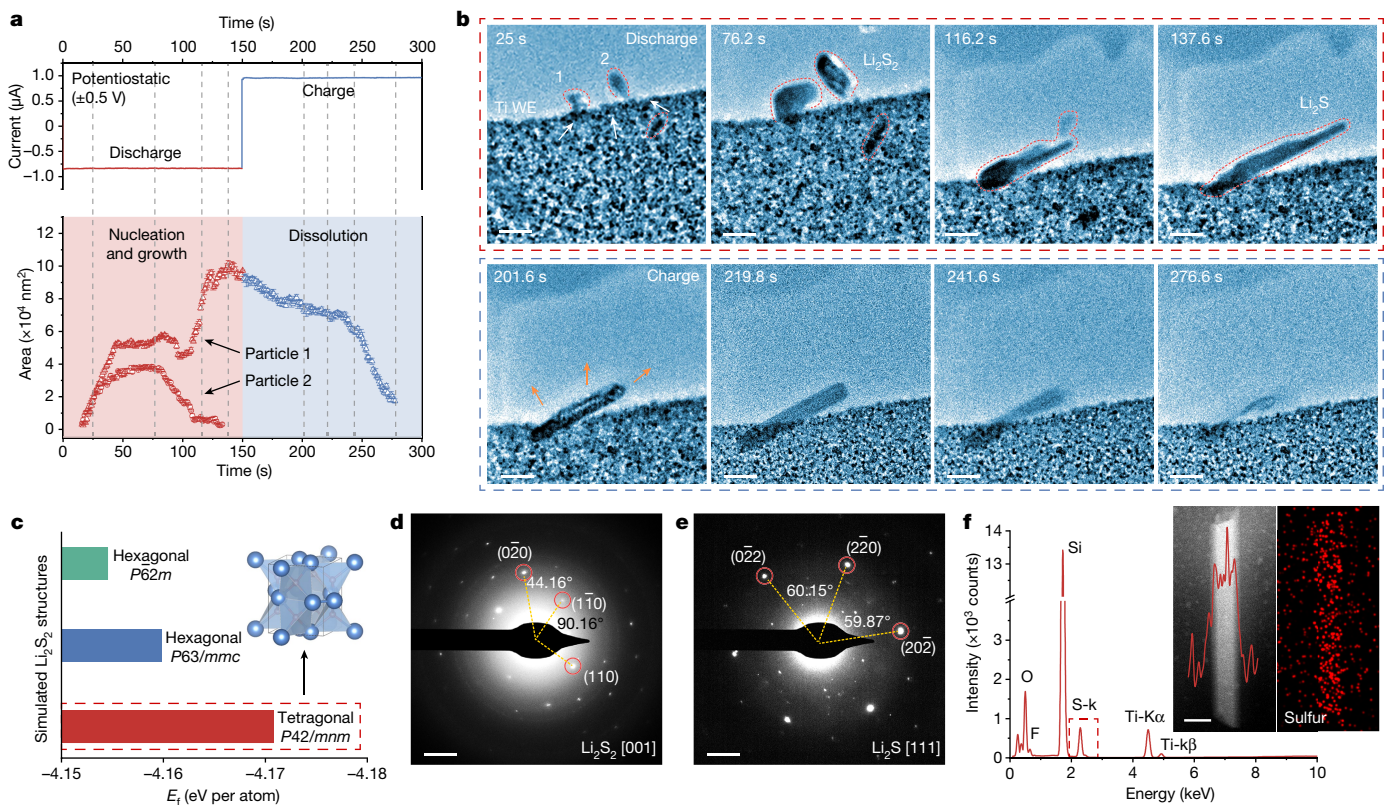


Fig. 2 | Interfacial reactions and structures of LiPSs without mediation of active centres. **a**, The applied electric field and the corresponding projection-area variation as a function of time of particles 1 and 2. The electrochemical liquid cell was first potentiostatically discharged at -0.5 V and then potentiostatically charged at $+0.5$ V for 150 s. Ten mM Li₂S₆ was used as the electrolyte. Error bars represent standard deviations of the measurement. **b**, Time-series TEM images from Supplementary Video 1 of Li₂S deposition (dashed red frame) and dissolution (dashed blue frame) in an electrochemical liquid cell. The white and orange arrows indicate the directions of charge transfer and diffusion of LiPSs, respectively. Scale bars, 200 nm. **c**, The energy

comparison between tetragonal $P4_2/mnm$ Li₂S₂ and hexagonal $P\bar{6}2m$ and $P6_3/mmc$ Li₂S₂. The inset is the crystal structure of the tetragonal Li₂S₂ unit cell with the lowest E_f , in which Li and S atoms are represented by red and blue balls, respectively. **d**, SAED pattern of granular Li₂S₂ (tetragonal, $P4_2/mnm$) along the [001] direction. Scale bar, 2 nm⁻¹. **e**, SAED pattern of rod-like Li₂S (cubic, $Fm\bar{3}m$) along the [111] direction. Scale bar, 2 nm⁻¹. **f**, EDS spectrum, STEM image and S element mapping of Li₂S. The corresponding TEM images of the SAED patterns of Li₂S₂ and Li₂S are provided in Supplementary Fig. 13. Scale bar, 200 nm. WE, working electrode.

attributed to the insulating property of Li₂S, leading to a large energy barrier at initial stages²⁶. Besides, rod-like Li₂S could also be directly deposited through a single-step pathway (Supplementary Fig. 11 and Supplementary Video 2). We also found that the reduced S_n²⁻ ($n \leq 2$) ions were diffusible, resulting in the precipitation of solid Li₂S_n ($n \leq 2$) near the electrode surface (Supplementary Fig. 12).

In situ EC-TEM results indicated that granular Li₂S₂ appeared as a metastable intermediate phase during discharge, making it hard to be captured. By simulating Li₂S₂ candidates with different crystal structures, we found that the tetragonal Li₂S₂ had the lowest formation energy (E_f) compared with that of multiple hexagonal Li₂S₂ (Fig. 2c and Extended Data Fig. 2a–c). The simulated and experimental selected-area electron diffraction (SAED) patterns were also highly consistent with the tetragonal Li₂S₂ structure along the [001] and [111] directions (Fig. 2d, Extended Data Fig. 2d,e and Supplementary Fig. 13). The above studies have resolved the controversial structure of the Li₂S₂ intermediate from both calculations and experiments^{16,27–30}. For rod-like Li₂S, SAED patterns indicated the [111], [011] and [100] directions of the face-centred cubic structure (Fig. 2e and Extended Data Fig. 2f). High-angle annular dark-field scanning transmission electron microscopy (HAADF-STEM) images and linear element distributions of energy-dispersive X-ray spectrometry (EDS) confirmed the uniform S distribution in the rod-like structure (Fig. 2f and Extended Data Fig. 2g).

We investigated various electrolyte concentrations and discharge potentials to understand the mechanism behind different deposition

pathways. Our results indicated that increasing the concentration of Li₂S₆ electrolyte (20 and 50 mM) did not affect the nucleation-growth pathway (Supplementary Fig. 14). However, changing the discharge potential resulted in distinct outcomes. At -0.5 V, granular and rod-like structures formed simultaneously (Supplementary Fig. 15), whereas at -0.1 V, solid discharge products primarily nucleated in granular structures, which transformed into rod-like/plate-like Li₂S as the deposition progressed (Extended Data Fig. 3 and Supplementary Video 3). The reaction at -0.1 V corresponds to a typical two-step deposition, which is also the main pathway of Li₂S deposition without active centres. According to the Lifshitz–Slyozov–Wagner model ($\text{area} \propto t^n$), the initial deposition at both -0.1 and -0.5 V followed a reaction-limited stage^{31–33} (Supplementary Fig. 16). This indicated that Li₂S deposition was predominantly controlled by the charge transfer at the electrode surface (Supplementary Fig. 17).

Collective pathway

To investigate the effect of metallic active centres in LiPSs redox reactions, Mo nanoclusters/N-doped graphene (Mo NCs/N-G) was rationally designed (for more details of the structure characterization of Mo NCs/N-G, see Methods, Fig. 3a–c and Supplementary Figs. 18–20). During potentiostatic discharge at -0.5 V (Fig. 3d and Supplementary Video 4), no nucleation/growth of rod-like Li₂S was observed (Extended Data Fig. 4a; 65/125 s), whereas Mo NCs/N-G nanosheet gradually spread

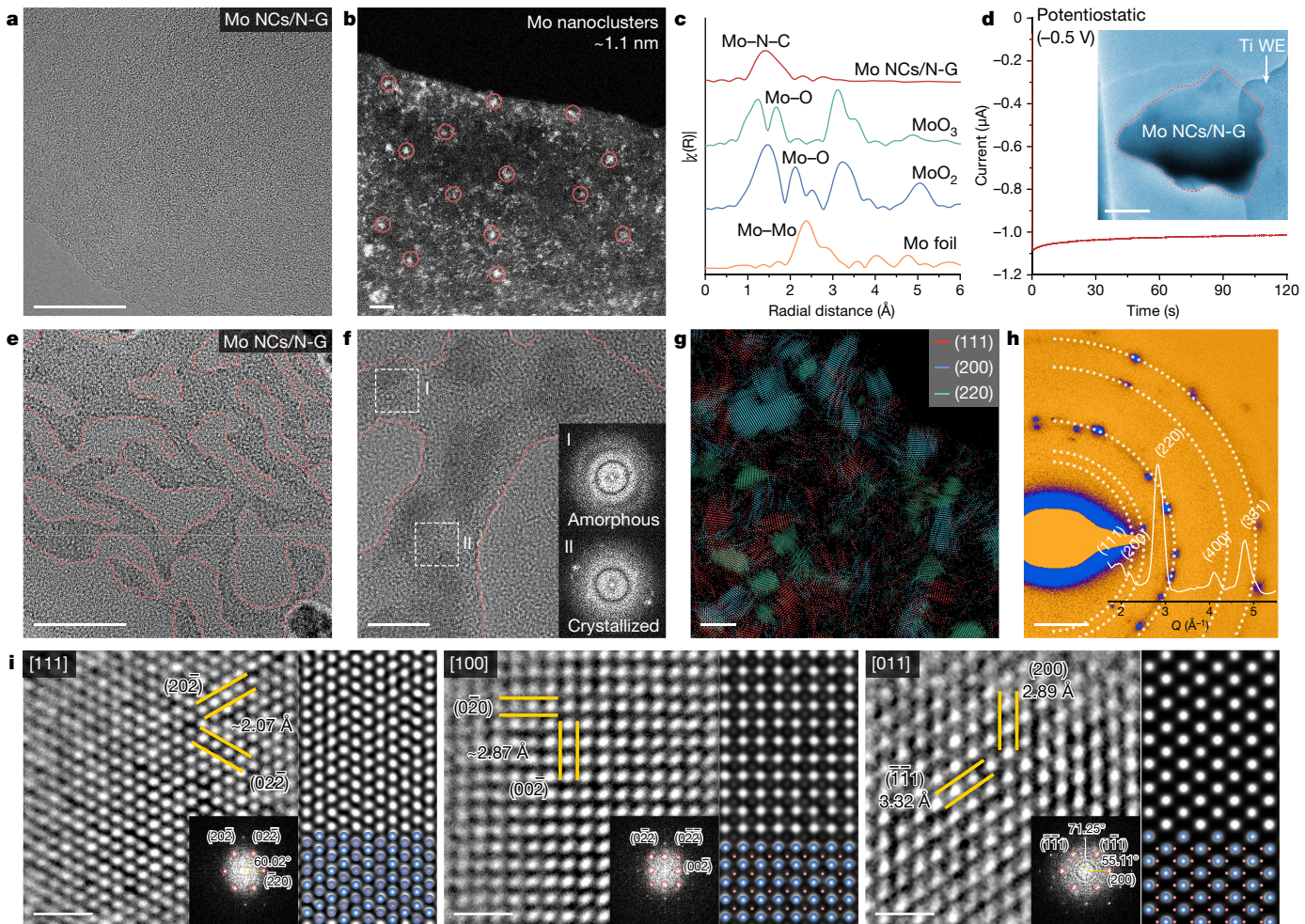


Fig. 3 | Structure of deposited Li_2S with mediation of active centres.

a, b, HRTEM and STEM images of Mo NCs/N-G showing the isolated Mo nanoclusters. Scale bars, 20 nm (a), 5 nm (b). **c,** Fourier transform of extended X-ray absorption fine structure in Rspace for Mo NCs/N-G and reference samples of Mo foil, MoO_3 and MoO_2 . **d,** The electric field applied to the observing area with potentiostatic discharge at -0.5 V. The inset TEM image is from Supplementary Video 4 using 10 mM Li_2S_6 as the electrolyte. Scale bar, 2 μm . **e, f,** HRTEM images of deposited Li_2S on Mo NCs/N-G after potentiostatic discharge at -0.5 V in an electrochemical liquid cell. Insets are the corresponding FFT patterns showing the amorphous and crystallized Li_2S in different areas. Scale bars, 20 nm (e), 10 nm (f). **g,** Inverse FFT patterns from HRTEM image in

Supplementary Fig. 23, showing that nanocrystalline Li_2S was mainly composed of (111), (200) and (220) crystal planes, represented by red, blue and green, respectively. Scale bar, 5 nm. **h,** SAED pattern and the corresponding intensity integration, showing the diffraction peaks of polycrystalline Li_2S . Q is the scattering vector calculated by $2\pi/d$, where d is the layer spacing. Scale bar, 2 nm^{-1} . **i,** Radial Wiener-filtered HRTEM images and FFT patterns of deposited nanocrystalline Li_2S along the [111], [100] and [011] directions. The corresponding simulated HRTEM images and models of the Li_2S supercell are shown on the right. Raw HRTEM images are provided in Supplementary Figs. 24 and 25. Scale bars, 1 nm. WE, working electrode.

out instead (185 s). Subsequent observation under a higher resolution revealed that many dark areas formed on the edge and surface of graphene during discharge (Extended Data Fig. 4b and Supplementary Video 5), corresponding to Li_2S deposition on Mo NCs/N-G nanosheet. Such a preferential reactivity of active centres was further confirmed in a higher-concentration electrolyte (100 mM Li_2S_6 ; Supplementary Video 6). Compared with bare electrode surface and Mo NCs/N-G nanosheet located at the bottom left without electronic contact, a distinct contrast variation was observed owing to the Li_2S deposition on Mo NCs/N-G nanosheet that was in direct contact with Ti electrode (highlighted by the dashed red frame in Extended Data Fig. 4c).

The structure of Li_2S was investigated at the atomic scale after the electrochemical deposition on Mo NCs/N-G nanosheet in liquid cells (for more details, see Supplementary Discussion 3, Extended Data Fig. 5 and Supplementary Fig. 21). The high-resolution transmission electron microscopy (HRTEM) image revealed that Li_2S was deposited in a nonequilibrium crystal form on Mo NCs/N-G nanosheet (Fig. 3e).

The deposited areas were composed of both nanocrystalline and amorphous Li_2S (Fig. 3f and Supplementary Fig. 22), in contrast to the single-crystalline face-centred cubic Li_2S deposited on the bare electrode surface. The spatial distribution of crystallized Li_2S domains was extracted by the inverse fast Fourier transform (FFT) frequencies of the HRTEM image (Fig. 3g and Supplementary Fig. 23), which revealed the randomly exposed crystal planes of nanocrystalline Li_2S . It was further confirmed by the polycrystalline diffraction rings of the SAED pattern (Fig. 3h). By comparing crystal structures between HRTEM images and simulated images (Fig. 3i and Supplementary Figs. 24 and 25), we could index the zone axis of face-centred cubic nanocrystalline Li_2S mainly along the [111], [100] and [011] directions (for more details of image acquisition and processing see Supplementary Discussion 4).

The interfacial reactions and reversibility of LiPSs mediated by active centres were further investigated under potentiostatic conditions at ± 0.5 V (Fig. 4a). Several droplet-like structures were formed during the first discharge at -0.5 V and Li_2S deposition at active-centre-mediated

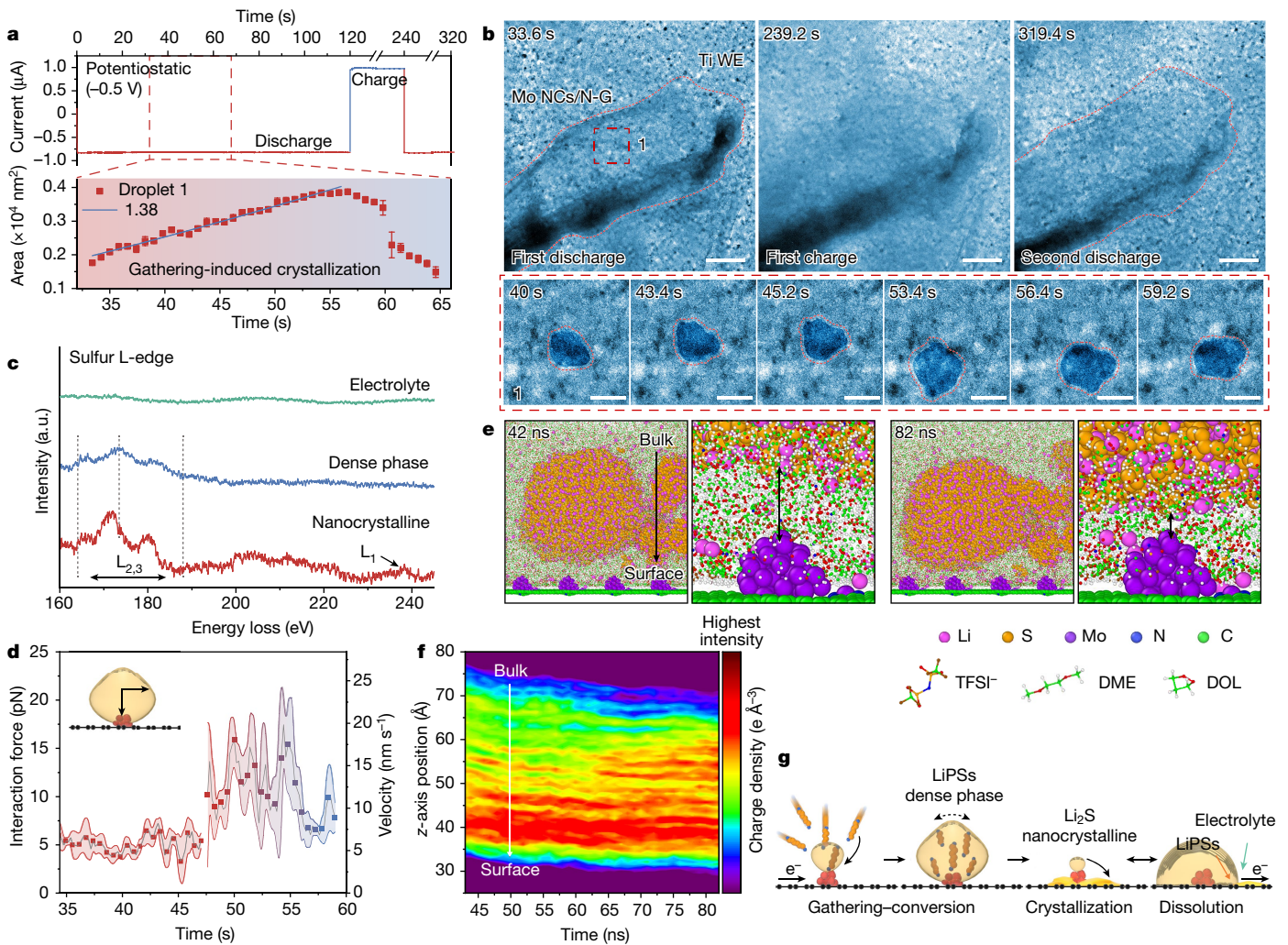


Fig. 4 | Interfacial redox reactions of LiPSs with mediation of active centres.

a, The applied electric field and the corresponding projection-area variation as a function of time of droplet 1 in **b**. The liquid cell underwent potentiostatic discharge–charge at ± 0.5 V, with 120 s for each step. Ten mM Li_2S_6 was used as the electrolyte. A power function was used to fit the area variation over time ($\text{area} \propto t^n$) according to the Lifshitz–Slyozov–Wagner model, in which $n \geq 1$ represents reaction-limited growth. Error bars represent standard deviations of the measurement. **b**, Time-series TEM images from Supplementary Video 7 showing the consecutive potentiostatic discharge–charge with mediation of active centres. Scale bars, 200 nm (top row), 50 nm (bottom row). **c**, EELS of the sulfur L-edge peaks of blank LiPSs electrolyte, droplet-like dense phase (area I, Extended Data Fig. 7a) and nanocrystalline Li_2S (area II, Extended Data Fig. 7b). **d**, Variation of interaction force and velocity of droplet 1. The overlapped areas in red and red-blue gradient colours are based on error bars showing the

standard deviation. The display point shown is every third data point collected. **e**, Time-series MD simulations showing the gathering of LiPSs by Mo active centres into a dense ion-complex phase consisting of Li^+ and S_6^{2-} with a Li_2S_6 concentration of 17.93 wt%. DFT calculated the charge quantity of Mo active centres ($Q = +7.37$ e). The z-axis distance between Mo active centres and the dense ion-complex phase decreased continuously during the simulation from 42 ns to 82 ns. The corresponding statistics are provided in Extended Data Fig. 8e. **f**, The charge-density variation of S_6^{2-} ions along the z axis as a function of time. The charge distribution of S_6^{2-} ions in the dense ion-complex phase was continuously enhanced from bulk to surface. **g**, Schematic illustration of interfacial reactions mediated by active centres, showing a gathering-induced collective charge transfer for Li_2S deposition. TFSI⁻, bis(trifluoromethanesulphonyl)imide; DOL, 1,3-dioxolane; DME, 1,2-dimethoxyethane. a.u., arbitrary units; WE, working electrode.

surface underwent gathering, conversion and crystallization (marked as droplets 1, 2 and 3; Fig. 4b, Extended Data Fig. 6a and Supplementary Video 7). Typically, for liquid droplet 1 (Extended Data Fig. 6b), it underwent continuous gathering and growth (40 s to 45.2 s). Subsequently, the droplet moved vigorously as it grew further (53.4 s to 59.2 s) but remained anchored on the active centre owing to the strong binding affinity towards LiPSs, rather than diffusing into electrolyte. According to the Lifshitz–Slyozov–Wagner model (Fig. 4a and Extended Data Fig. 6c), the gathering of liquid droplets 1, 2 and 3 followed a reaction-limited process, indicating that the charge transfer was the rate-limiting step. After that, rapid deposition of Li_2S from the droplets of LiPSs occurred within 5 s and a similar spreading and edge-roughening of Mo NCs/N-G nanosheet was observed (Extended

Data Fig. 6c). During redox reactions, the surface of Mo NCs/N-G was observed to be periodically clear and blurry (239.2 s and 319.4 s; Fig. 4b), corresponding to the reversible solid–liquid phase transformation of LiPSs mediated by active centres.

The droplet-like structures were analysed. The irregular and ever-changing edges, along with low contrast, indicate that these structures are not crystallized or nucleated $\text{Li}_2\text{S}_2/\text{Li}_2\text{S}$ but highly concentrated Li_2S_n ($2 < n \leq 6$) gathered by active centres. According to the literature, a dense liquid phase could form through a liquid–liquid phase segregation, triggered by concentration difference^{34,35}. This phenomenon is thermodynamically favourable and can considerably reduce the surface free energy relative to the solution–crystal interfaces^{36,37}. HRTEM images along with their FFT and SAED patterns revealed the structures

of droplet-like dense phase and Li₂S nanoparticles (Extended Data Fig. 7a,b), whereas HAADF-STEM images and EDS mappings confirmed a high concentration of sulfur in the dense phase. In electron energy loss spectra (EELS; Fig. 4c), the sulfur L_{2,3} and L₁ edge peaks should be located at 162–185 eV and 238 eV, respectively^{23,24}. These peaks were absent in the bulk electrolyte but were found in the dense phase with two peaks at 173.5 eV and 180.7 eV. The sulfur L-edge peaks in nanocrystalline Li₂S were substantially stronger and showed a chemical redshift compared with the dense phase, which should be attributed to the electrochemical reduction from S_n²⁻ ($2 < n \leq 6$) to S²⁻. The formation of several droplets on the surface of Mo NCs/N-G nanosheets was further confirmed by HRTEM images and Z-contrast analysis of HAADF-STEM images (Extended Data Fig. 7c–f and Supplementary Figs. 26 and 27).

Interaction of active centres with LiPSs was commonly attributed to the chemical bonding^{2,3}. However, the interaction could be more complex at the nanoscale/microscale, probably involving electrostatic force, van der Waals force and surface molecular force^{38,39}. To quantitatively analyse the interfacial reaction of the dense phase of LiPSs, we tracked the centroid motion of droplet 1 and used the Einstein–Stokes equation to calculate the interaction force (F , pN) and velocity (v , nm s⁻¹) of droplet 1 towards active centres over time (Fig. 4d and Extended Data Fig. 6b,d). Our results showed that the strong interaction between active centres and LiPSs stabilized the droplet-like dense phase during initial gathering (overlapped in red). Subsequently, droplet 1 experienced a continuous waggle on the surface, which should be ascribed to the simultaneous gathering and electrochemical reduction of S_n²⁻ ($2 < n \leq 6$, overlapped in red–blue gradient). Finally, the drift velocity decreased gradually before reaching the threshold for instantaneous crystallization. *In situ* observation showed that droplet-like dense phase was grabbed by active centres and the size could reach a diameter of around 30 nm, indicating a long-range and strong interaction.

Simulations and calculations

To understand the formation and transformation mechanism of droplet-like dense phase, we established MD models to study the reaction dynamics of LiPSs. Comparing the electrode surfaces of Mo NCs/N-G and Ti, our simulations showed that Mo active centres were able to attract S_n²⁻ from the bulk solution, independent of electrolyte concentration (Extended Data Fig. 8a–c, Supplementary Figs. 28–30 and Supplementary Video 8). Statistical analysis indicated a stronger long-range attraction towards S_n²⁻ ions of Mo active centres than the Ti surface (Extended Data Fig. 8d). MD simulation and z-axis position analysis showed that the dense phase composed of S_n²⁻ and Li⁺ ion complex continuously approached the Mo NCs/N-G surface (Fig. 4e, Extended Data Fig. 8e and Supplementary Video 9). By contrast, the Ti surface showed no interaction with LiPSs (Supplementary Fig. 31a and Supplementary Video 10), despite DFT calculations indicating that Ti (001) had a higher adsorption energy towards Li₂S_n than Mo active centres (Supplementary Fig. 31b). This suggests that the Ti surface can only provide the strong chemical bonding but poor long-range interaction towards LiPSs. By analysing mean square displacement (MSD) curves along the z axis (Extended Data Fig. 8f), we found that the diffusion coefficient of droplet-like dense phase at the Mo NCs/N-G surface was enhanced by two orders of magnitude compared with that of the Ti surface. DFT calculations showed that the charge of metallic Mo centre was +7.37 e (Supplementary Fig. 31c). Therefore, the strong interaction between Mo active centres and droplets of LiPSs should be attributed to electrostatic force. Analysis of the charge of S_n²⁻ ions in the dense ion-complex phase showed a dynamic variation over time and became more concentrated from bulk to surface along the z axis (Fig. 4f and Supplementary Fig. 31d). The charge transfer between Mo active centres and Li₂S_n was investigated by ab initio molecular dynamics (AIMD) simulations. By comparing the charge distribution of several Li₂S_n molecules in the dense phase before and after applying

an electrode potential, we found that electrons were transferred and shared from Mo active centres to polysulfide ions in the dense phase, from internal to external layers, rather than only the Li₂S_n molecules close to the active centres (Extended Data Fig. 8g; for more details of simulations, see Supplementary Discussion 5). The investigations confirm that the long-range gathering effect of Mo active centres induces the formation of droplet-like dense phases and then these droplets work as integral reaction units, allowing charge transfer among S_n²⁻ ions.

Electrochemical investigations

To validate the reactions of LiPSs over different surfaces, we conducted parallel investigation on the discharge products in coin-type cells, the gathering of soluble LiPSs and their fast conversion into solid Li₂S, which were confirmed by *ex situ* characterizations (for more details, see Supplementary Discussion 6 and Supplementary Figs. 32–34). Potentiostatic discharge coin-type cells showed faster reaction kinetics and higher Li₂S deposition capacity with the mediation of active centres (Extended Data Fig. 9a), which were 1,410 s ahead of peak current and 2.4 times higher in capacity. Electrochemical impedance spectroscopy (EIS) revealed a much smaller charge-transfer resistance after Li₂S deposition (6.9 ohm versus 132.7 ohm; Extended Data Fig. 9b and Supplementary Fig. 35a) and higher reversibility in the subsequent Li₂S dissolution with active centres (Extended Data Fig. 9c). The activation energy (E_a) was markedly reduced during the liquid–solid transformation of LiPSs (Extended Data Fig. 9d,e and Supplementary Fig. 36). In symmetric cells (Extended Data Fig. 9f and Supplementary Fig. 35b), Mo NCs/N-G demonstrated a smaller potential gap of the redox peaks (0.67 V versus 0.82 V) and ten times higher current density. Galvanostatic tests of Mo NCs/N-G and Ti electrode showed a 2.07 times higher capacity-retention rate with active centres (Extended Data Fig. 9g). Specifically, the initial redox reaction of LiPSs revealed a much lower nucleation/dissolution barrier and voltage polarization, and the potential barrier of Li₂S dissolution almost vanished starting from the second cycle (Extended Data Fig. 9h,i). Furthermore, the application potential of Mo active centres in Li–S full cells was demonstrated under realistic working conditions, including high mass loading, fast charging and lean electrolyte conditions (for more details of electrochemical performance, see Methods and Extended Data Fig. 10).

Discussion

During multielectron reactions of Li–S batteries, the adsorption, catalysis and conversion between intermediates of LiPSs and active centres are involved and the complexity of reaction kinetics governing Li₂S deposition/dissolution leads to diverse and ambiguous pathways. In this work, by using high temporal–spatial resolution *in situ* EC-TEM, we showed that active centres gathered soluble LiPSs into droplet-like dense phase and thus induced an instantaneous crystallization, rather than a classical step-by-step transformation. Besides, our preliminary results indicate that the collective reaction mechanism seems to be universal to other metal active centres, which needs more systematic investigations. Previous studies of material/surface modification mainly focused on clarifying the adsorption and catalysis mechanism from a single-molecule aspect. Our experiment and simulation results indicated that the aggregation state and collective behaviour of ions and molecules played a critical role in the kinetics of electrochemical interfacial reactions. The collective mechanism provides new insight into constructing next-generation, high-energy, long-life and fast-charging Li–S batteries.

Online content

Any methods, additional references, Nature Portfolio reporting summaries, source data, extended data, supplementary information,

acknowledgements, peer review information; details of author contributions and competing interests; and statements of data and code availability are available at <https://doi.org/10.1038/s41586-023-06326-8>.

1. Ji, X., Lee, K. T. & Nazar, L. F. A highly ordered nanostructured carbon–sulphur cathode for lithium–sulphur batteries. *Nat. Mater.* **8**, 500–506 (2009).
2. Zhao, C. et al. A high-energy and long-cycling lithium–sulfur pouch cell via a macroporous catalytic cathode with double-end binding sites. *Nat. Nanotechnol.* **16**, 166–173 (2021).
3. Peng, L. et al. A fundamental look at electrocatalytic sulfur reduction reaction. *Nat. Catal.* **3**, 762–770 (2020).
4. Shen, Z. et al. Cation-doped ZnS catalysts for polysulfide conversion in lithium–sulfur batteries. *Nat. Catal.* **5**, 555–563 (2022).
5. Chen, H. et al. Catalytic materials for lithium–sulfur batteries: mechanisms, design strategies and future perspective. *Mater. Today* **52**, 364–388 (2021).
6. Liu, Y. et al. Electrolyte solutions design for lithium–sulfur batteries. *Joule* **5**, 2323–2364 (2021).
7. Liang, Z. et al. Advances in the development of single-atom catalysts for high-energy-density lithium–sulfur batteries. *Adv. Mater.* **34**, e2200102 (2022).
8. Rehman, S., Pope, M., Tao, S. & McCalla, E. Evaluating the effectiveness of in situ characterization techniques in overcoming mechanistic limitations in lithium–sulfur batteries. *Energy Environ. Sci.* **15**, 1423–1460 (2022).
9. Ross, F. M. Opportunities and challenges in liquid cell electron microscopy. *Science* **350**, aaa9886 (2015).
10. Zeng, C. et al. Dynamic investigation of battery materials via advanced visualization: from particle, electrode to cell level. *Adv. Mater.* **34**, e2200777 (2022).
11. Kong, L. et al. Current-density dependence of Li₂S/Li₂S₂ growth in lithium–sulfur batteries. *Energy Environ. Sci.* **12**, 2976–2982 (2019).
12. Zhao, G.-X., Ahmed, W. H. Z. & Zhu, F.-L. Nitrogen-sulfur co-doped porous carbon preparation and its application in lithium–sulfur batteries. *J. Electrochem.* **27**, 614–623 (2021).
13. Pei, F. et al. A two-dimensional porous carbon-modified separator for high-energy-density Li–S batteries. *Joule* **2**, 323–336 (2018).
14. Tsao, Y. et al. Designing a quinone-based redox mediator to facilitate Li₂S oxidation in Li–S batteries. *Joule* **3**, 872–884 (2019).
15. Nelson, J. et al. In operando X-ray diffraction and transmission X-ray microscopy of lithium sulfur batteries. *J. Am. Chem. Soc.* **134**, 6337–6343 (2012).
16. Cuisinier, M. et al. Sulfur speciation in Li–S batteries determined by operando X-ray absorption spectroscopy. *J. Phys. Chem. Lett.* **4**, 3227–3232 (2013).
17. Li, M. et al. Evidence of morphological change in sulfur cathodes upon irradiation by synchrotron X-rays. *ACS Energy Lett.* **7**, 577–582 (2022).
18. See, K. A. et al. Ab initio structure search and in situ ⁷Li NMR studies of discharge products in the Li–S battery system. *J. Am. Chem. Soc.* **136**, 16368–16377 (2014).
19. Chen, J.-J. et al. Conductive Lewis base matrix to recover the missing link of Li₂S₈ during the sulfur redox cycle in Li–S battery. *Chem. Mater.* **27**, 2048–2055 (2015).
20. Sun, X. et al. Dislocation-induced stop-and-go kinetics of interfacial transformations. *Nature* **607**, 708–713 (2022).
21. Frey, H. et al. Dynamic interplay between metal nanoparticles and oxide support under redox conditions. *Science* **376**, 982–987 (2022).
22. Kim, H. et al. In situ TEM observation of electrochemical lithiation of sulfur confined within inner cylindrical pores of carbon nanotubes. *Adv. Energy Mater.* **5**, 1501306 (2015).
23. Wang, Z. et al. In situ TEM observations of discharging/charging of solid-state lithium–sulfur batteries at high temperatures. *Small* **16**, 2001899 (2020).
24. Xu, Z.-L. et al. Visualization of regulated nucleation and growth of lithium sulfides for high energy lithium sulfur batteries. *Energy Environ. Sci.* **12**, 3144–3155 (2019).
25. Seo, H. K. et al. Direct visualization of lithium polysulfides and their suppression in liquid electrolyte. *Nano Lett.* **20**, 2080–2086 (2020).
26. Zhang, L. et al. Revealing the electrochemical charging mechanism of nanosized Li₂S by in situ and operando X-ray absorption spectroscopy. *Nano Lett.* **17**, 5084–5091 (2017).
27. Conder, J. et al. Direct observation of lithium polysulfides in lithium–sulfur batteries using operando X-ray diffraction. *Nat. Energy* **2**, 17069 (2017).
28. Yang, G., Shi, S., Yang, J. & Ma, Y. Insight into the role of Li₂S₂ in Li–S batteries: a first-principles study. *J. Mater. Chem. A* **3**, 8865–8869 (2015).
29. Feng, Z. et al. Unravelling the role of Li₂S in lithium–sulfur batteries: a first principles study of its energetic and electronic properties. *J. Power Sources* **272**, 518–521 (2014).
30. Paoletta, A. et al. Transient existence of crystalline lithium disulfide Li₂S₂ in a lithium–sulfur battery. *J. Power Sources* **325**, 641–645 (2016).
31. Wagner, C. Theory of precipitate change by redissolution. *Z. Elektrochem.* **65**, 581–591 (1961).
32. Lifshitz, I. M. & Slyozov, V. V. The kinetics of precipitation from supersaturated solid solutions. *J. Phys. Chem. Solids* **19**, 35–50 (1961).
33. Viswanatha, R. & Sarma, D. D. in *Nanomaterials Chemistry* (eds Rao, C. N. R., Müller, A., Cheetham, A. K.) 139–170 (Wiley, 2007).
34. Gower, L. B. & Odum, D. J. Deposition of calcium carbonate films by a polymer-induced liquid-precursor (PILP) process. *J. Cryst. Growth* **210**, 719–734 (2000).
35. Smeets, P. J. et al. Calcium carbonate nucleation driven by ion binding in a biomimetic matrix revealed by in situ electron microscopy. *Nat. Mater.* **14**, 394–399 (2015).
36. Wallace, A. F. et al. Microscopic evidence for liquid–liquid separation in supersaturated CaCO₃ solutions. *Science* **341**, 885–889 (2013).
37. De Yoreo, J. J. et al. Crystallization by particle attachment in synthetic, biogenic, and geologic environments. *Science* **349**, aaa6760 (2015).
38. Min, Y. J. et al. The role of interparticle and external forces in nanoparticle assembly. *Nat. Mater.* **7**, 527–538 (2008).
39. Bishop, K. J., Wilmer, C. E., Soh, S. & Grzybowski, B. A. Nanoscale forces and their uses in self-assembly. *Small* **5**, 1600–1630 (2009).

Publisher's note Springer Nature remains neutral with regard to jurisdictional claims in published maps and institutional affiliations.

Springer Nature or its licensor (e.g. a society or other partner) holds exclusive rights to this article under a publishing agreement with the author(s) or other rightsholder(s); author self-archiving of the accepted manuscript version of this article is solely governed by the terms of such publishing agreement and applicable law.

© UChicago Argonne, LLC, Operator of Argonne National Laboratory 2023

Methods

Sample synthesis

Synthesis of $(\text{NH}_4)_{42}[\text{Mo}^{\text{VI}}_{72}\text{Mo}^{\text{V}}_{60}\text{O}_{372}(\text{CH}_3\text{COO})_{30}\cdot(\text{H}_2\text{O})_{72}]$ polyoxometalates (Mo_{132} POMs). $(\text{NH}_4)_{42}[\text{Mo}^{\text{VI}}_{72}\text{Mo}^{\text{V}}_{60}\text{O}_{372}(\text{CH}_3\text{COO})_{30}\cdot(\text{H}_2\text{O})_{72}]$ was synthesized following the previously reported method⁴⁰. Specifically, 4.5 mmol $(\text{NH}_4)_6\text{Mo}_7\text{O}_{24}\cdot 4\text{H}_2\text{O}$ and 162.2 mmol $\text{CH}_3\text{COONH}_4$ was dissolved in 250 ml deionized water under stirring. 6.1 mmol $\text{N}_2\text{H}_4\cdot\text{SO}_4$ was added to this solution, followed by further stirring for 10 min. Then, 83 ml CH_3COOH (50%, v/v) was added. The obtained solution was transferred to an Erlenmeyer flask and left to stand at 20 °C for 4 days. The product was washed by ethanol and diethyl ether several times, followed by subsequent drying to obtain reddish-brown crystals.

Synthesis of ethylenediamine-functionalized reduced graphene oxide (EDA-rGO). GO was chemically exfoliated from graphite according to the modified Hummers method⁴¹. First, the nucleophilic ring-opening reaction of epoxy groups was used to immobilize the amino group on it and, at the same time, rGO was obtained owing to the removal of oxygen-containing groups. Specifically, 60 mg GO nanosheets was uniformly dispersed in 60 ml deionized water and 120 μl EDA was added under vigorous stirring. The homogeneous solution was transferred to a Teflon-lined stainless-steel autoclave, heating at 75 °C for 6 h. After cooling to room temperature naturally, the product was washed by deionized water several times, followed by subsequent freeze-drying, and EDA-rGO was obtained.

Synthesis of Mo NCs/N-G and N-G. Mo NCs/N-G was mainly prepared by the electrostatic interaction between negatively charged Mo_{132} POMs and positively charged EDA-rGO (protonated), which were strongly coupled to form the Mo_{132} POMs/EDA-rGO. The steric confinement and monomolecular dispersion properties of POMs in the Mo_{132} POMs/EDA-rGO composite favoured the formation of atomically dispersed active sites during thermal annealing. Specifically, 30 mg EDA-rGO was ultrasonically dispersed in 30 ml deionized water for 0.5 h, followed by vigorous stirring. Then, the pH value of EDA-rGO solution was adjusted to 4.0 with the addition of 120 μl 1 M HCl solution. Meanwhile, 3 mg Mo_{132} POMs was uniformly dispersed in 30 ml deionized water and dropwise added into EDA-rGO solution. After continuous stirring for 12 h, the product was washed by deionized water several times, followed by subsequent freeze-drying, and Mo_{132} POMs/EDA-rGO was obtained. Mo_{132} POMs/EDA-rGO was annealed at 750 °C for 1 h under Ar atmosphere with a heating rate of 10 °C min⁻¹, and Mo NCs/N-G was finally obtained.

Synthesis of Mo NCs/N-G/S. Mo NCs/N-G/S was prepared through a sulfur melt-diffusing process. Specifically, Mo NCs/N-G was mixed with sulfur at the weight ratio of 1:4 by sufficient grinding. The homogeneous mixture was heated at 155 °C under Ar atmosphere for 12 h. After natural cooling to room temperature, it was taken out and ground, followed by reheating under the same conditions to uniformly composite with sulfur.

Structure characterization

The morphology and element distribution of Mo NCs/N-G was characterized by an FEI Talos F200S microscope equipped with a Super-X EDS system and FEI Themis Z G2 30-300 with both image and probe correctors. Dual EELS were acquired for the electrolyte, droplet-like dense phase and nanocrystalline Li_2S in electrochemical liquid cells using a Titan G2 (S)TEM operated at 60–300 kV with an energy resolution of 0.8 eV. The raw EELS were processed by background removement (power law) and plural scattering removement (Fourier ratio). The chemical environment and bonding information were detected by X-ray photoelectron spectroscopy (PHOIBOS150). The powder crystalline structure of Mo NCs/N-G and Li_2S deposited electrodes was

investigated by XRD with Cu-K α radiation (Bruker D8 A25; $\lambda = 1.5418 \text{ \AA}$). X-ray absorption fine-structure spectra at the Mo K edge were acquired by a Si (111) monochromator at beamline 20-BM of the Advanced Photon Source. The beamline energy resolution was about $\Delta E/E = 1.3 \times 10^{-4}$. X-ray absorption spectroscopy data were processed using the ATHENA and ARTEMIS software packages. The weight ratio of metallic Mo nano-clusters was measured by inductively coupled plasma optical emission spectroscopy (Agilent 720ES). After the disassembly of the coin-type cells in an argon-filled glovebox and transferring to a tailor-made device to prevent air pollution, ex situ characterizations were conducted. Laser confocal Raman spectra were collected on a Nanophoton spectrometer (laser source: 532 nm, 600 gr mm⁻¹, ND = 180, exposure time = 5 s). The optical absorbance spectra were analysed by ultraviolet-visible spectroscopy (Shimadzu UV-3600). The morphology was characterized by field-emission scanning electron microscopy (ZEISS).

In situ liquid-cell EC-TEM experiment set-up and observation

The in situ EC-TEM holder was purchased from Chip-Nova and liquid cells were custom made. Two silicon wafers were used as bottom and top chips, on which an observation window of 10-nm-thick low-stress SiN_x membrane was constructed. Ti working electrode and counter/reference electrodes were deposited on the bottom chip with a face-to-face distance of 200 μm . Before assembly of the bottom and top chips, Mo NCs/N-G was transferred onto the Ti electrodes of the bottom chip. The bare chips were also assembled to study LiPSs transformation without mediation of active centres. Electrolyte was prepared by mixing 10/20/50/100 mM Li_2S_6 (S and Li_2S , molar ratio: 5:1) in 1 M lithium bis(trifluoromethanesulphonyl)imide (LiTFSI) in 1,3-dioxolane (DOL)/1,2-dimethoxyethane (DME) (v/v = 1:1) electrolyte, followed by stirring overnight. The entire processes of electrolyte injection and chip sealing were performed in the Ar-filled glovebox ($\text{H}_2\text{O} < 0.01 \text{ ppm}$, $\text{O}_2 < 0.01 \text{ ppm}$). Ether-based electrolyte was added to a reservoir using a syringe, which would flow into the observation window by capillary force, and then epoxy was used to seal the liquid cell. The sealed liquid cell needed to stand for 12 h to stabilize the internal solution environment. Then, the liquid cell was placed into a custom-made EC-TEM holder and an electric field was applied by an electrochemical workstation (CHI 660E). The in situ EC-TEM experiment was performed in an FEI Talos microscope with an acceleration voltage of 200 kV. To avoid the influence of e-beam effect, the e-beam dose rate was controlled to be below 1.5 e $\text{\AA}^{-2} \text{ s}^{-1}$ for in situ electrochemical experiments. Multislice simulation was conducted to simulate HRTEM images of nanocrystalline Li_2S acquired in an electrochemical liquid cell^{42,43}. A self-written MATLAB script was used to build the crystal models of Li_2S along the [111], [100] and [011] directions. HRTEM images were simulated on the basis of the following parameters: accelerating voltage 200 kV, spherical aberration coefficient $C_s = 1.2 \text{ mm}$, chromatic aberration coefficient $C_c = 1.5 \text{ mm}$, sample thickness around 5 nm and defocus $\Delta f = 40 \text{ nm}$.

Electrochemical measurements

Potentiostatic deposition and dissolution of Li_2S . 100 mM Li_2S_6 prepared as above was used as the electrolyte for Li_2S potentiostatic nucleation. Slurry was prepared by ball milling the mixture of 80 wt% sulfur-free electrode material (Mo NCs/N-G) and 20 wt% LA133 aqueous binder, which was then coated on Ti mesh discs (16 mm in diameter). The areal loading of active material was controlled at around 0.5 mg cm⁻². For cell assembly, 20 μl 100 mM Li_2S_6 electrolyte was added to the cathode side and 20 μl of regular electrolyte (1 M LiTFSI in 1:1 (v/v) DOL/DME) was added to the Li anode side. The assembled cells were galvanostatically discharged to 2.06 V at 0.112 mA and then kept potentiostatically at 2.05 V for the nucleation and growth of Li_2S until the current was below 0.01 mA. For Li_2S dissolution, the cells were further galvanostatically discharged to 1.8 V at 0.01 mA and then kept potentiostatically at 2.4 V until the current was below 0.01 mA. The capacity of deposited Li_2S was calculated according to Faraday's law.

Activation energy. The coin-type cells were galvanostatically discharged to specific discharge potentials at $16 \mu\text{A cm}^{-2}$ with $100 \text{ mM Li}_2\text{S}_6$ electrolyte. The cells were held at the same potential, using chronoamperometry, until a stable output current was achieved. EIS was tested at the frequency range from 100 kHz to 10 mHz from 2.0 to 1.7 V using a Multi Autolab M204 electrochemical workstation.

Symmetry cells. CV symmetric cells, both with and without active centres, were collected and compared at a scan rate of 0.1 mV s^{-1} , ranging from -1.0 to 1.0 V . The electrodes decorated with Mo NCs/N-G nanosheets were further tested at increasing scan rates from 0.1 to 1 mV s^{-1} .

Li–S batteries. The slurry was prepared by ball milling the mixture of 80 wt\% electrode material (Mo NCs/N-G/S), 10 wt\% acetylene black and 10 wt\% LA133 aqueous binder (15 wt\% , aqueous dispersion of acrylonitrile copolymer). The uniform slurry was coated on aluminium foil, drying at $60 \text{ }^\circ\text{C}$ for 10 h in vacuum. The cathode was cut into a disc with an areal loading of 1.13 cm^2 (12 mm in diameter). The sulfur areal loading was controlled at around 2 mg cm^{-2} for cycling performance at $1/2/3 \text{ C}$ and rate performance. For high sulfur loading test at 0.2 C , the slurry was coated on the self-standing carbon-nanofibre-based electrode prepared by electrospinning, with sulfur areal loading of $2, 3.5, 5.4$ and 7 mg cm^{-2} . The electrolyte is about 17.7 (2 mg cm^{-2}) and 10.1 (3.5 mg cm^{-2}) $\mu\text{l mg}^{-1}$ for regular cells and 4.3 (5.4 mg cm^{-2}) and 5.1 (7 mg cm^{-2}) for high-loading cells. Coin-type cells were used for electrochemical performance (CR2032). Mo NCs/N-G/S cathode was assembled with Li anode, ether-based electrolyte and polypropylene separators (Celgard 2325) in an argon-filled glovebox. 1 M LiTFSI in $1:1$ (v/v) DOL/DME with 2 wt\% LiNO_3 was used as the electrolyte. The electrochemical tests were carried out on a Neware battery cycler (CT-4008T-5V20mA-164) with a voltage window of 1.8 – 2.8 V versus Li/Li^+ . All electrochemical tests were carried out at room temperature.

Interaction force between active centres and droplet-like dense phase

The MSD of a randomly diffusing molecular is proportional to its diffusing time ($\text{MSD} = nDt$), in which D is the diffusion coefficient. For *in situ* EC-TEM study in a liquid cell, the molecular diffusion is considered in a two-dimensional space (three-dimensional space $n = 6$, two-dimensional space $n = 4$), so the MSD relation gives^{44,45}:

$$\text{MSD} = 4Dt \quad (1)$$

The diffusion coefficient of droplet-like dense phase was estimated by tracking its centroid movement in Fig. 4b. The two-dimensional moving trajectory and edge-variation profile are shown in Extended Data Fig. 6b. According to the MSD as a function of time (equation (1) and Extended Data Fig. 6d), the diffusion coefficient ($D = 4.71 \text{ nm}^2 \text{ s}^{-1}$) of droplet 1 was obtained by a linear fit, which was similar to other reported *in situ* TEM studies of Li–S batteries^{32,34}. The difference in diffusion coefficient calculated from MSD curves between *in situ* TEM results and MD simulations should be attributed to the following reasons. (1) The observed droplets from *in situ* TEM was in the dozens of nanometres scale. By contrast, MD simulation focused on ion-complex groups in the few nanometres scale, so the diffusion and movement were intensified. (2) The thin liquid layer in electrochemical liquid cells also limited the motion rate of LiPSs droplets.

In the limit of low Reynolds number, we measured the velocity and interaction force of the droplet-like structure. For a nearly spherical droplet with a constant radius R , the interaction force F is proportional to the drag coefficient γ , and the Stokes' law gives:

$$F = \gamma v = (6\pi\eta R)v \quad (2)$$

in which η is the viscosity of electrolyte (s m^{-2}) and v is the velocity of droplet-like structure (nm s^{-1}). The mobility μ is the inverse of the

drag coefficient γ . According to the Einstein relation ($D = \mu k_B T / q$), the diffusion coefficient is proportional to its mobility constant. The Einstein–Stokes equation can be given as:

$$D = k_B T / 6\pi\eta R \quad (3)$$

in which k_B is the Boltzmann constant ($1.38 \times 10^{-23} \text{ J K}^{-1}$) and T is temperature (300 K). Substituting the drag coefficient γ of a nearly spherical droplet-like structure from Stokes' law, the interaction force F can be calculated as follows:

$$F = (k_B T / D)v \quad (4)$$

The calculated interaction force and velocity between active centres and droplet 1 is shown in Fig. 4d.

Methods of DFT calculation

To determine the experimentally observed Li_2S_2 crystal structure, tetragonal Li_2S_2 structure and various hexagonal Li_2S_2 structures were constructed for stability analysis. Hexagonal Li_2S_2 was constructed on the basis of hexagonal A_2B_2 candidates, including Li_2O_2 , Na_2O_2 , Na_2S_2 , Na_2Se_2 , K_2O_2 , K_2S_2 and Rb_2S_2 (Extended Data Fig. 2a–d). N-doped graphene containing Mo nanoclusters with different sizes (unit cell size: $17.09 \text{ \AA} \times 17.22 \text{ \AA} \times 22 \text{ \AA}$) was considered as the theoretical model for the calculation of monomer adsorption strength. The model contained 106 C atoms and four N atoms (with a two-atom defect site for anchoring the Mo nanoclusters in Mo NCs/N-G), in which the Mo nanoclusters contained one, four and nine Mo atoms, respectively. The spin-polarized DFT calculations were carried out by using the Vienna Ab initio Simulation Package (VASP.5.4.4)⁴⁶. The correlation energy and exchange energy were calculated by using the Perdew–Burke–Ernzerhof form of the generalized gradient approximation⁴⁷. The cutoff energy of the plane wave was 500 eV . The number of k points in the Brillouin zone multiplied by the lattice parameter in each dimension was approximately 20. The structural optimization was carried out at a convergence of 0.01 eV \AA^{-1} on the force. Furthermore, the semiempirical van der Waals correction method of Grimme et al. (DFT-D3) was used to describe the dispersion interaction⁴⁸.

The formation energy (E_f) of different Li_2S_2 structures was calculated by:

$$E_f = E_{\text{crystal}}/n \quad (5)$$

in which E_{crystal} is the total energy of the Li_2S_2 cell and n is the total atoms of the unit cell. The adsorption energy of monomers ($E_{\text{ads-monomer}}$) on each graphene slab was calculated by:

$$E_{\text{ads-monomer}} = E_{\text{total}} - E_{\text{monomer}} - E_{\text{slab}} \quad (6)$$

in which E_{total} is the total energy of the Mo NCs/N-G slab with one adsorbed monomer molecule, E_{monomer} is the energy of an isolated monomer molecule and E_{slab} is the energy of the Mo NCs/N-G slab.

The Mo NCs/N-G model with a four-atom Mo nanocluster was used to investigate the charge transfer between the electrodes and LiPSs (Extended Data Fig. 8g). A solution layer containing three Li_2S_6 , three LiTFSI , 12 DOL and 12 DME molecules was constructed on the surface of Mo NCs/N-G electrode. As reported by Le et al.⁴⁹, the electrode potential was simulated by adding six Li atoms under the Mo NCs/N-G, and these Li atoms would not diffuse into the vacuum layer or solution during the simulation. All models were charge neutral and the charges of ions were provided by Bader charge analysis. The electronic structure of the interface was analysed after a relaxation of 20 ps in the NVT ensemble and after applying the electrode potential for 8 ps (Extended Data Fig. 8g). The hybrid Gaussian and plane waves method as implemented in the Quickstep module of the CP2K package⁵⁰ was used for

Article

AIMD simulations. The Perdew–Burke–Ernzerhof functional with the Grimme et al. D3 van der Waals correction method was used to calculate the Li diffusion. The Goedecker, Teter and Hutter pseudopotentials combined with the DZVP-MOLOPT-SR-GTH basis set was used for all atoms⁵¹. To speed up the structure relaxation, the H atoms in the system were changed to D atoms, and the time step was set as 1 fs. Owing to the large cell size, only the Γ point in the Brillouin zone was used for calculations. The second-generation Car–Parrinello molecular dynamics (SGCPMD)^{52,53} was used for model optimization sampling and the system temperature was set at 350 K. The Langevin friction coefficient (γ_l) was set to 0.001 fs⁻¹ and the region friction coefficients (γ_b) of Mo and other atoms were set to 5×10^5 fs⁻¹ and 2.1×10^4 fs⁻¹, respectively.

Methods and models of MD simulation

To investigate the diffusion and aggregation behaviours of Li_2S_6 in the bulk solution, random filling models were constructed with different Li_2S_6 concentrations of 2.51 wt%, 5.28 wt%, 9.68 wt% and 17.93 wt% (Extended Data Fig. 8a and Supplementary Figs. 24 and 25). The solution was filled with 255 LiTFSI, 1,020 DOL and 1,020 DME molecules. To study the interaction between Li_2S_6 molecules and various electrodes (Mo NCs/N-G and Ti), MD models of a solution layer on the electrode surface were constructed (Extended Data Fig. 8c and Supplementary Fig. 26). The Mo NCs/N-G model, which consisted of defective N-doped graphene-supported nanoclusters containing 40 Mo atoms and had a box size of $98.4 \text{ \AA} \times 76.695 \text{ \AA} \times 200 \text{ \AA}$, was constructed from the optimized unit cell shown in Supplementary Fig. 27c. The Ti model was a six-layer Ti (001) slab of the hcp phase, possessing a lattice parameter of 2.93 \AA , and was constructed with a box size similar to that of the Mo NCs/N-G model. To simulate different concentrations of Li_2S_6 on the electrode surfaces, 65, 125 and 255 Li_2S_6 molecules were randomly introduced into a solution composed of 255 LiTFSI, 1,020 DOL and 1,020 DME molecules. These quantities corresponded to the Li_2S_6 concentrations of 5.28 wt%, 9.68 wt% and 17.93 wt%, respectively. To investigate the interaction mechanism between dense ion-complex phases composed of Li^+ and S_6^{2-} and various electrodes of Mo NCs/N-G and Ti (Fig. 4e and Supplementary Fig. 27a), MD models were further expanded by increasing the simulation box size to $172.2 \text{ \AA} \times 153.39 \text{ \AA} \times 250 \text{ \AA}$. The models comprise 3,060 Li_2S_6 molecules in a solution consisting of 1,020 LiTFSI, 4,080 DOL and 4,080 DME in a layered compact state. The models were developed to simulate the high-concentration Li_2S_6 -enriched region on the electrode surface.

All MD simulations were performed using the Large-scale Atomic/Molecular Massively Parallel Simulator (LAMMPS) software package⁵⁴. Lennard-Jones 12-6 (LJ12-6) potential and electrostatic potential were used to describe the nonbonded interactions between particles in the system:

$$U_{ij}(r_{ij}) = 4\epsilon_{ij} \left[\left(\frac{\sigma_{ij}}{r_{ij}} \right)^{12} - \left(\frac{\sigma_{ij}}{r_{ij}} \right)^6 + \frac{1}{4\pi\epsilon_0} \frac{q_i q_j}{r_{ij}} \right] \quad (7)$$

in which the subscript ij represents the interaction between particles i and j , U_{ij} represents the potential energy generated by the interaction, r_{ij} represents the distance between the particles and q_i is the charge on atom i . The LJ interaction parameters were calculated using the Lorentz–Berthelot combining rules ($\sigma_{ij} = (\sigma_i + \sigma_j)/2$; $\epsilon_{ij} = \sqrt{\epsilon_i \epsilon_j}$). Periodic boundary conditions in the x and y directions and nonperiodic boundary conditions in the z direction were used in all interfacial simulations. Furthermore, the nonbonded parameters and force constants of bonds, angles and dihedrals of DME and DOL molecules were derived from the OPLS-AA force field⁵⁵, whereas that of LiTFSI was extracted from the literature⁵⁶. Meanwhile, we used the force-field parameters reported by Hu et al. for Li_2S_6 molecules⁵⁷. The parameters of Mo NCs/N-G used for the LJ interaction referred to the work of Bernardes et al. (for Mo) and Abbaspour et al. (for N and C), respectively^{58,59}. For the atomic

charges of the Mo NCs/N-G model, it followed the Bader charge analysis of the unit cell optimized by the above DFT calculations. The LJ interaction parameters of Ti referred to the report by Jacobson et al.⁶⁰.

In all simulations, the equations of motion were integrated using a time step of 1 fs and temperature control was achieved by coupling LiTFSI, Li_2S_6 , DOL and DME molecules to a Nosé–Hoover thermostat with a time constant of 0.1 ps (refs. 61,62), respectively. All atoms of the electrode slabs were fixed throughout the simulations.

To investigate the diffusion and aggregation behaviours of Li_2S_6 molecules in the bulk solution at various concentrations, the simulation programme involved a relaxation phase of 2 ns at a pressure of 1 bar in the NPT ensemble, followed by a 90-ns NVT ensemble simulation for sampling. The clusters of S atoms whose distance from each other in the solution was less than 3.5 Å were identified and counted every 10 ps to obtain the cluster size (Extended Data Fig. 8b). The five largest S_6^{2-} clusters in the simulated system were selected and their sizes were averaged to evaluate the aggregation of S_6^{2-} ions. To investigate the interaction between the different electrode surfaces (Mo NCs/N-G and Ti) and Li_2S_6 molecules, the simulation programme involved an initial relaxation phase in the NVT ensemble for 2 ns to fully optimize the randomly constructed solution layer. This was then followed by a 90-ns simulation for sampling. The number of S atoms on different electrode surfaces was counted every 10 ps within the area of z coordinate 0–15 Å (Extended Data Fig. 8d). The high-concentration interface layers were initially relaxed at 500 K for 2 ns in the canonical ensemble. Subsequently, the temperatures were gradually lowered to 300 K to continue the simulations for 40 ns over the Mo NCs/N-G (Fig. 4e) and Ti (Supplementary Fig. 27a) surfaces. To facilitate a better comparison of interfacial diffusion, relevant statistics were gathered during the subsequent 40-ns simulations at a temperature of 350 K (specifically, between 42 ns and 82 ns; Extended Data Fig. 8e). To compare the difference in S_6^{2-} migration across different electrode interfaces, we calculated the MSD of Li_2S_6 along the z axis (Extended Data Fig. 8f):

$$\text{MSD} - Z = \langle (z - z_0)^2 \rangle = \frac{1}{N} \sum_{n=1}^N (z_n(t) - z_n(0))^2 \quad (8)$$

in which N is the number of S atoms of Li_2S_6 in the simulation box, $z_n(t)$ is the z position of each S atom at time t and $z_n(0)$ is the reference z position of each S atom.

To investigate the redistribution of S_6^{2-} ions near the electrode induced by the Mo active centres, the simulation box was divided into slices of 0.5 Å thickness. The number of S_6^{2-} ions in each slice was computed every 10 ps and the average number of S_6^{2-} ions in each slice was recorded every 1 ns to calculate the charge density of S_6^{2-} ions, as shown in Fig. 4f and Supplementary Fig. 27d:

$$\rho_Q = \frac{q_{\text{S}_6} \times \sum_z^{z+0.5} n_{\text{S}_6}}{V_{\text{slice}}} \quad (9)$$

in which q_{S_6} is the charge of one S_6^{2-} ion (that is, 2), n_{S_6} is the total number of S_6^{2-} ions in the slice with a thickness of 0.5 Å in the z direction and V_{slice} is the volume of the slice.

Structure characterization of Mo NCs/N-G

The nanocluster active-centre-immobilized surface, Mo NCs/N-G nanosheet, was designed for the following considerations: high reactivity of atomically isolated metal sites and easy integration on liquid-cell electrodes for high-resolution observation. Mo NCs/N-G was prepared by coupling the negatively charged POMs with positively charged amino groups of graphene, which ensured the monodispersed distribution and isolated anchoring of POMs (Supplementary Fig. 18). The HRTEM image and XRD pattern revealed the amorphous structure of Mo NCs/N-G nanosheet (Fig. 3a and Supplementary Fig. 19a). The

HAADF-STEM image further confirmed the monodispersed Mo nano-clusters, with an average size of 1.1 nm and a content of 6.9 wt% (Fig. 3b and Supplementary Fig. 19b,c). In XANES, the absorption energy of Mo NCs/N-G was between $\text{MoO}_3/\text{MoO}_2$ and Mo foil, indicating a positively charged active centre (Supplementary Fig. 19d). X-ray photoelectron spectroscopy detected three main peak regions corresponding to the valence states of Mo^0 , Mo^{+4} and Mo^{+6} (Supplementary Fig. 19e). The XANES linear combination fitting showed that the percentages of these valence states were 10%, 57% and 33%, respectively (Supplementary Fig. 20). Fourier transform of extended X-ray absorption fine structure showed that the strongest peak of Mo NCs/N-G was located at about 1.4 Å (Fig. 3c), which indicates that Mo atoms were mainly bonded to N atoms (Supplementary Fig. 19f).

Electrochemical performance of Li-S full cells

Electrochemical performance of Mo NCs/N-G/S with high sulfur loading (80 wt%) was investigated under high mass loading, fast charging and lean electrolyte conditions. Mo NCs/N-G/S exhibited a cycling performance of 887 mA h g⁻¹ at 1 C for 100 cycles and rate capability of 1,525, 1,127, 1,018, 942, 879, 766 and 639 mA h g⁻¹ at 0.1, 0.2, 0.5, 1, 2, 3 and 4 C, respectively (Extended Data Fig. 10a–c). At the increasing sulfur areal loading of 2, 3.5, 5.4 ($E/S = 4.3 \mu\text{l mg}^{-1}\text{s}$) and 7 mg cm⁻² ($5.1 \mu\text{l mg}^{-1}\text{s}$), it delivered the areal capacities of 2.3, 3.9, 5.5 and 6.6 mA h cm⁻² over 40 cycles, respectively (Extended Data Fig. 10d). At 2 and 3 C, it delivered discharge capacities of 645 and 573 mA h g⁻¹ after 500 cycles with low-capacity decay of 0.038% and 0.047% per cycle, respectively (Extended Data Fig. 10e).

Data availability

The data that support the findings of this study are available from the corresponding authors on reasonable request.

40. Müller, A. et al. Organizational forms of matter: an inorganic super fullerene and keplerate based on molybdenum oxide. *Angew. Chem. Int. Ed.* **37**, 3360–3363 (1998).
41. Hummers, W. S. & Offeman, R. E. Preparation of graphitic oxide. *J. Am. Chem. Soc.* **80**, 1339 (1958).
42. Cowley, J. M. & Moodie, A. F. The scattering of electrons by atoms and crystals. I. A new theoretical approach. *Acta Crystallogr.* **10**, 609–619 (1957).
43. Goodman, P. & Moodie, A. F. Numerical evaluations of N-beam wave functions in electron scattering by the multi-slice method. *Acta Crystallogr.* **A30**, 280–290 (1974).
44. Liao, H.-G., Cui, L., Whitelam, S. & Zheng, H. Real-time imaging of Pt_xFe nanorod growth in solution. *Science* **336**, 1011–1014 (2012).
45. Zheng, H. et al. Nanocrystal diffusion in a liquid thin film observed by in situ transmission electron microscopy. *Nano Lett.* **9**, 2460–2465 (2009).
46. Kresse, G. & Furthmüller, J. Efficiency of ab-initio total energy calculations for metals and semiconductors using a plane-wave basis set. *Comput. Mater. Sci.* **6**, 15–50 (1996).
47. Perdew, J. P., Burke, K. & Ernzerhof, M. Generalized gradient approximation made simple. *Phys. Rev. Lett.* **77**, 3865–3868 (1996).
48. Grimme, S., Antony, J., Ehrlich, S. & Krieg, H. A consistent and accurate *ab initio* parametrization of density functional dispersion correction (DFT-D) for the 94 elements H–Pu. *J. Chem. Phys.* **132**, 154104 (2010).
49. Le, J.-B., Fan, Q.-Y., Li, J.-Q. & Cheng, J. Molecular origin of negative component of Helmholtz capacitance at electrified Pt(111)/water interface. *Sci. Adv.* **6**, eabb1219 (2020).
50. Hutter, J., Iannuzzi, M., Schiffmann, F. & VandeVondele, J. CP2K: atomistic simulations of condensed matter systems. *Wiley Interdiscip. Rev. Comput. Mol. Sci.* **4**, 15–25 (2014).
51. Jain, A. et al. Commentary: The Materials Project: a materials genome approach to accelerating materials innovation. *APL Mater.* **1**, 011002 (2013).
52. Kühne, T. D., Krack, M., Mohamed, F. R. & Parrinello, M. Efficient and accurate Car-Parrinello-like approach to Born-Oppenheimer molecular dynamics. *Phys. Rev. Lett.* **98**, 066401 (2007).
53. Lan, J., Hutter, J. & Iannuzzi, M. First-principles simulations of an aqueous CO/Pt(111) interface. *J. Phys. Chem. C* **122**, 24068–24076 (2018).
54. Dodda, L. S., Vaca, I., C. D., Tirado-Rives, J. & Jorgensen, W. L. Fast parallel algorithms for short-range molecular dynamics. *J. Comput. Phys.* **117**, 1–19 (1995).
55. Dodda, L. S., Cabeza de Vaca, I., Tirado-Rives, J. & Jorgensen, W. L. LigParGen web server: an automatic OPLS-AA parameter generator for organic ligands. *Nucleic Acids Res.* **45**, W331–W336 (2017).
56. Zhang, Y. et al. Water-in-salt LiTFSI aqueous electrolytes. I. Liquid structure from combined molecular dynamics simulation and experimental studies. *J. Phys. Chem. B* **125**, 4501–4513 (2021).
57. Hu, T. et al. Understanding structural and transport properties of dissolved Li₂S_n in ionic liquid electrolytes through molecular dynamics simulations. *ChemPhysChem* **22**, 419–429 (2021).
58. Abbaspour, M., Akbarzadeh, H. & Zaeifi, S. Thermodynamics, structure, and dynamic properties of nanostructured water confined into B-, N-, and Si-doped graphene surfaces and carbon nanotubes. *Ind. Eng. Chem. Res.* **59**, 9642–9654 (2020).
59. Bernardes, C. E., Canongia Lopes, J. N. & Minas da Piedade, M. E. All-atom force field for molecular dynamics simulations on organotransition metal solids and liquids. Application to M(CO)_n (M = Cr, Fe, Ni, Mo, Ru, or W) compounds. *J. Phys. Chem. A* **117**, 11107–11113 (2013).
60. Jacobson, D. W. & Thompson, G. B. Revisting Lennard Jones, Morse, and N-M potentials for metals. *Comp. Mater. Sci.* **205**, 111206 (2022).
61. Hoover, W. G. Canonical dynamics: equilibrium phase-space distributions. *Phys. Rev. A* **31**, 1695–1697 (1985).
62. Nosé, S. A molecular dynamics method for simulations in the canonical ensemble. *Mol. Phys.* **52**, 255–268 (2006).

Acknowledgements This work was supported by the Fundamental Research Funds for the Central Universities (202720220009) and National Natural Science Foundation of China (grants nos. 22288102, 22021001, U22A20396, 32101217, 21991151, 2191150 and 91934303). Research at the Argonne National Laboratory was financed by the US Department of Energy (DOE), Vehicle Technologies Office. Support from T. Duong of the US DOE's Vehicle Technologies Office programme is gratefully acknowledged. This research used resources of the Advanced Photon Source, a US Department of Energy (DOE) Office of Science user facility operated for the DOE Office of Science by Argonne National Laboratory under contract no. DE-AC02-06CH11357. G.-L.X. and K.A. also acknowledge the support from Clean Vehicles, US-China Clean Energy Research Center (CERC-CVC2). This research also employed the resources of the Shanghai Synchrotron Radiation Facility (SSRF), under contract no. 2021-SSRF-ZD-000730, 2022-SSRF-PT-019758 and 2022-SSRF-PT-021637, Hefei National Synchrotron Radiation Laboratory (NSRL-USTC, under contract no. 2021-HLS-PT-004529), and Beijing Synchrotron Radiation Laboratory (under contract no. 2021-BEPC-PT-005760 and 2022-BEPC-PT-006478). S.Z. is thankful for the support from Xiamen University Nanqiang Cultivation Program for Outstanding Doctoral Students. We thank Y. Cheng and M.-S. Wang (College of Materials, Xiamen University) and S. Li and C.-G. Shi (College of Chemistry and Chemical Engineering, Xiamen University) for helpful discussions and suggestions on *in situ* TEM, Raman and XRD characterizations.

Author contributions S.-G.S., H.-G.L., G.-L.X. and K.A. conceived and supervised this work. S.Z. designed the experiments, conducted TEM, materials synthesis, electrochemistry and wrote the paper. J.S. conducted the DFT calculations and MD simulations. J.-F.C., Y.Q., Y.L. and L.H. participated in discussions and data analysis. S.L., G.L. and Y.C. conducted the TEM characterization. F.P. and Q.Z. measured the electrochemical performance. C.Z., I.H. and C.-J.S. conducted XAS characterization. J.D. fabricated electrochemical liquid cells. J.L. and Y.D. conducted EELS characterization. All authors participated in the analysis of experimental data and discussion of the results, as well as in the writing and revision of the manuscript.

Competing interests The authors declare no competing interests.

Additional information

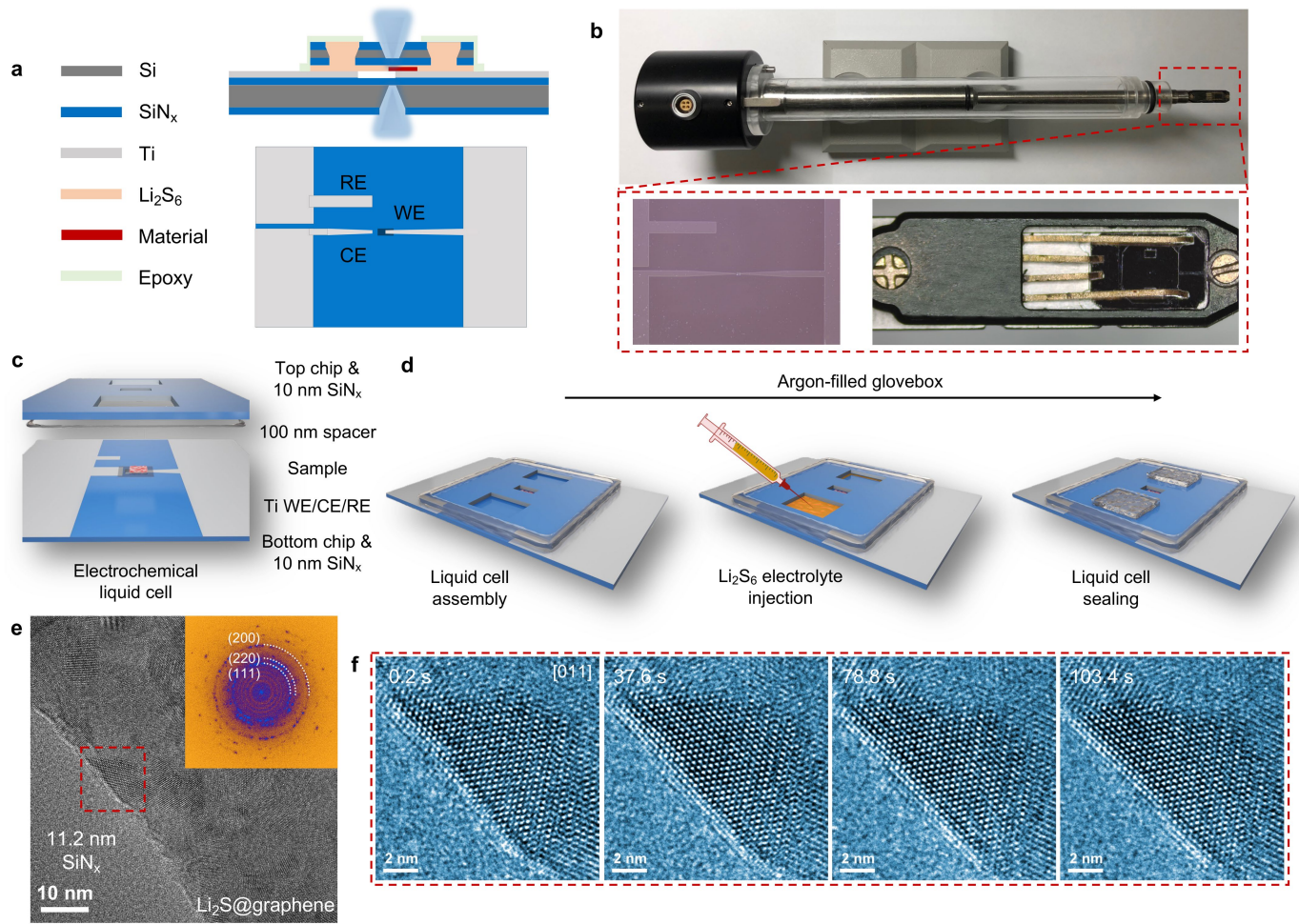
Supplementary information The online version contains supplementary material available at <https://doi.org/10.1038/s41586-023-06326-8>.

Correspondence and requests for materials should be addressed to Gui-Liang Xu, Khalil Amine or Hong-Gang Liao.

Peer review information *Nature* thanks Hyun-Wook Lee, Yongfu Tang and the other, anonymous, reviewer(s) for their contribution to the peer review of this work. Peer review reports are available.

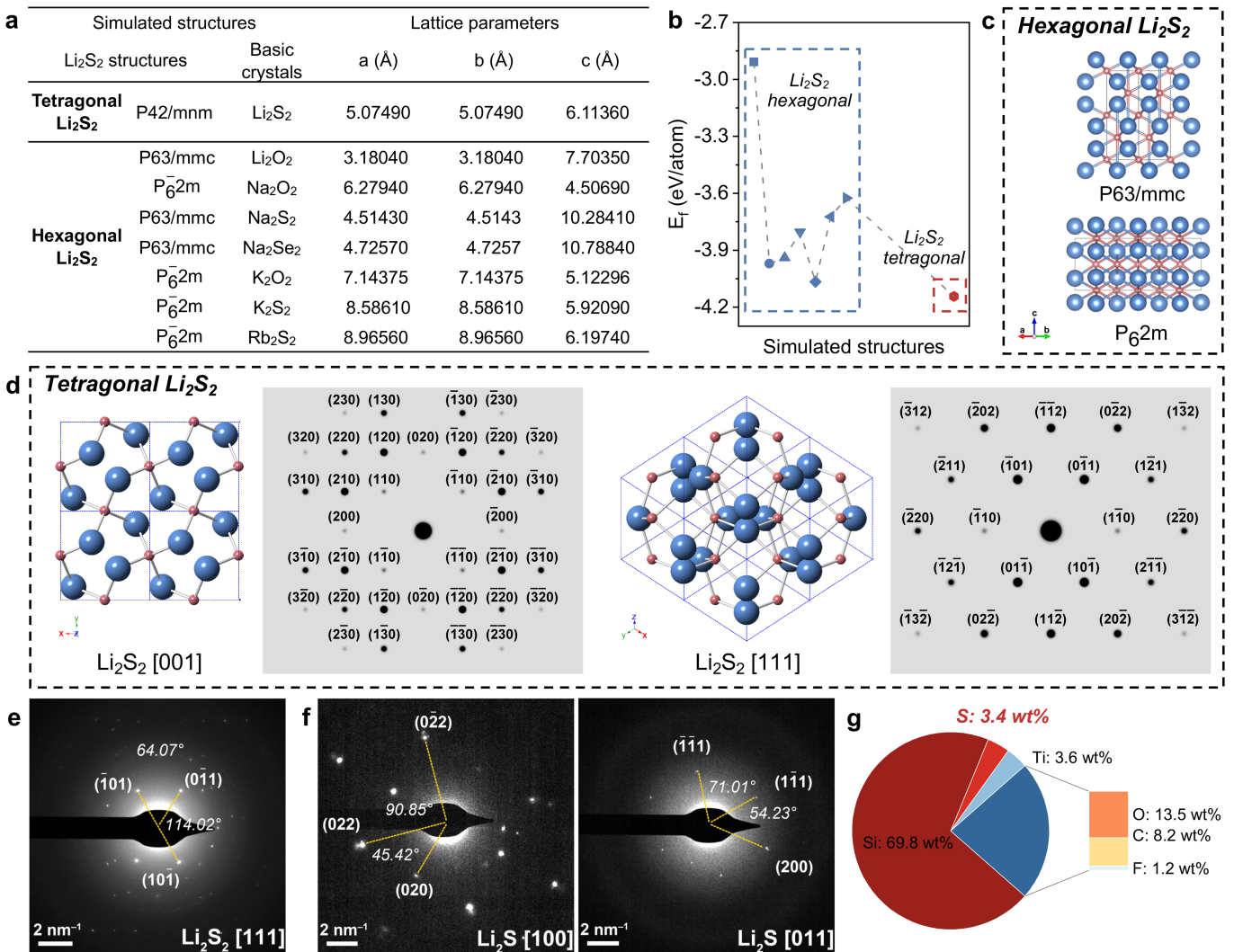
Reprints and permissions information is available at <http://www.nature.com/reprints>.

Article



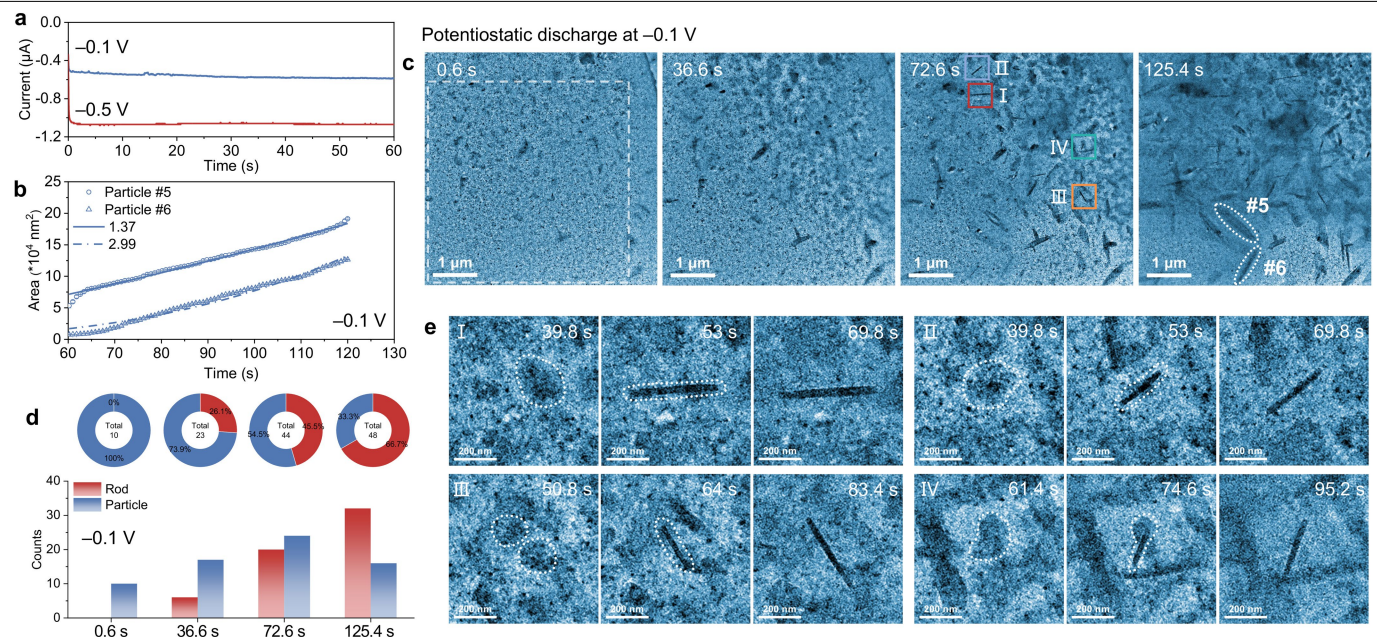
Extended Data Fig. 1 | Configuration of the liquid-cell EC-TEM. **a**, Schematic illustration of an electrochemical liquid cell from the top and side views, composed of top/bottom chips with 10-nm SiN_x observation windows, 100-nm spacers and samples on electrodes. **b**, Digital photographs of EC-TEM holder and electrochemical liquid cell. **c,d**, Schematic process of liquid-cell preparation in an argon-filled glovebox. After liquid-cell assembly, the pre-prepared Li₂S₆ electrolyte with various concentrations was injected and filled by capillary

force, before being sealed with epoxy. **e**, HRTEM image and corresponding FFT pattern of Li₂S@graphene loaded on a single bottom chip with 11.2-nm SiN_x layers. The thickness of the SiN_x layers was measured using a spectroscopic ellipsometer with a spectral range of 193–1,000 nm. **f**, Time-series HRTEM images of Li₂S@graphene (dashed red frame) showing the high spatial resolution and stable atomic structure at a dose rate of 18,200 e Å⁻²s⁻¹.



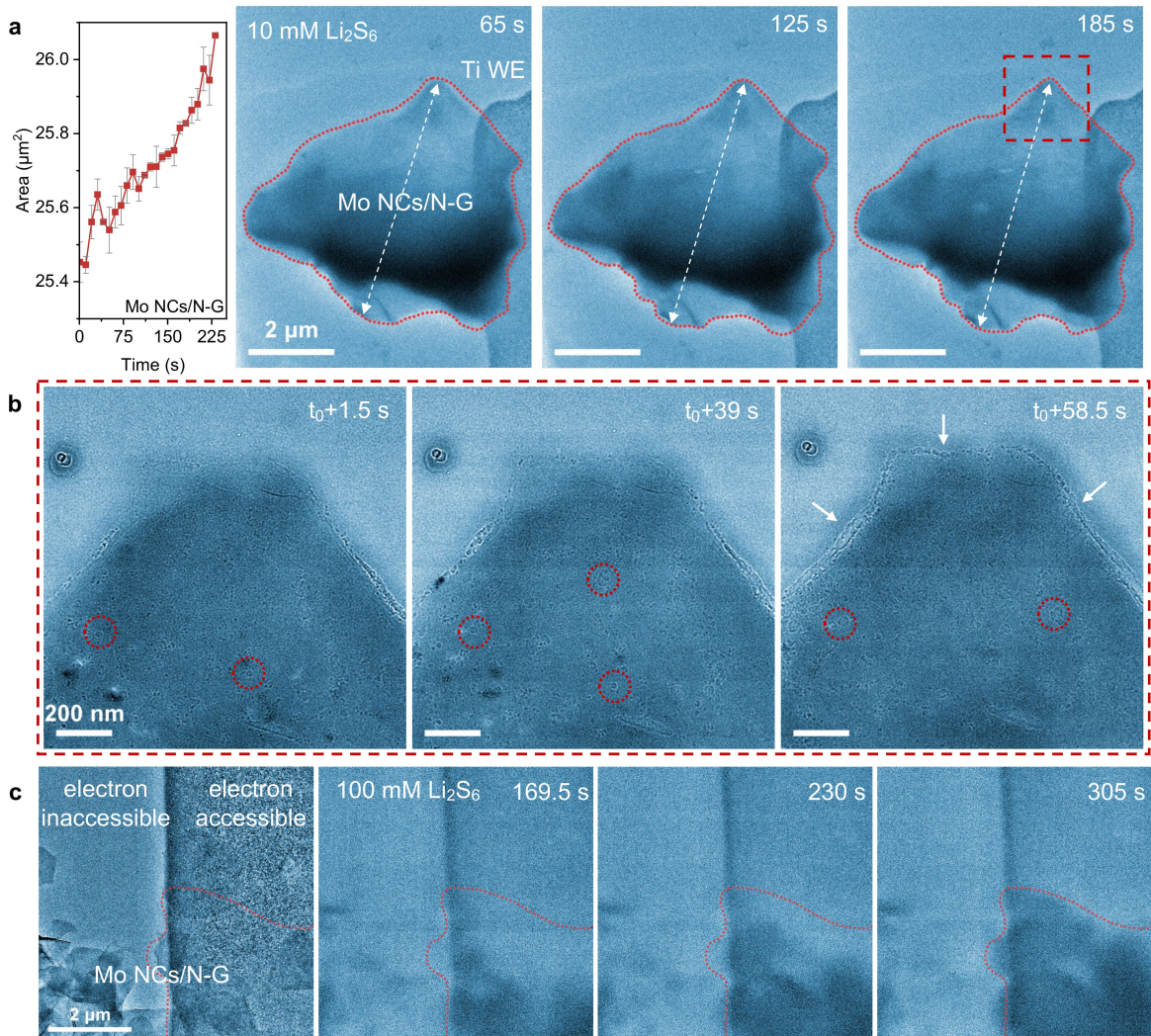
Extended Data Fig. 2 | Crystal structure of the simulated Li₂S₂. **a**, The fixed lattice parameters of tetragonal Li₂S₂ and hexagonal Li₂S₂ simulated on the basis of several hexagonal A₂B₂ structures. **b**, The corresponding energy comparison between tetragonal Li₂S₂ and hexagonal Li₂S₂. The hexagonal Li₂S₂ structures were constructed on the basis of Li₂O₂, Na₂O₂, Na₂S₂, Na₂Se₂, K₂O₂, K₂S₂ and Rb₂S₂, arranged from left to right in the dashed blue frame. **c**, The simulated crystal structures of hexagonal Li₂S₂ with P63/mmc and P₆2m space groups. **d**, The crystal structures and simulated electron diffraction of

tetragonal Li₂S₂ along the [001] and [111] directions, respectively. The abnormal systematic extinction of electron diffraction in Fig. 2d, that is, the appearance of (100) and (300), should be attributed to the lattice defect of Li₂S₂, which led to the diffraction deviating from the Bragg condition, and the secondary diffraction occurred. **e**, SAED pattern of granular Li₂S₂ (tetragonal, P4₂/mnm) along the [111] direction. **f**, SAED patterns of rod-like Li₂S (cubic, Fm $\bar{3}m$) along the [100] and [011] directions. **g**, Elemental weight ratio according to EDS spectrum in Fig. 2f. The red and blue balls represent Li and S atoms, respectively.



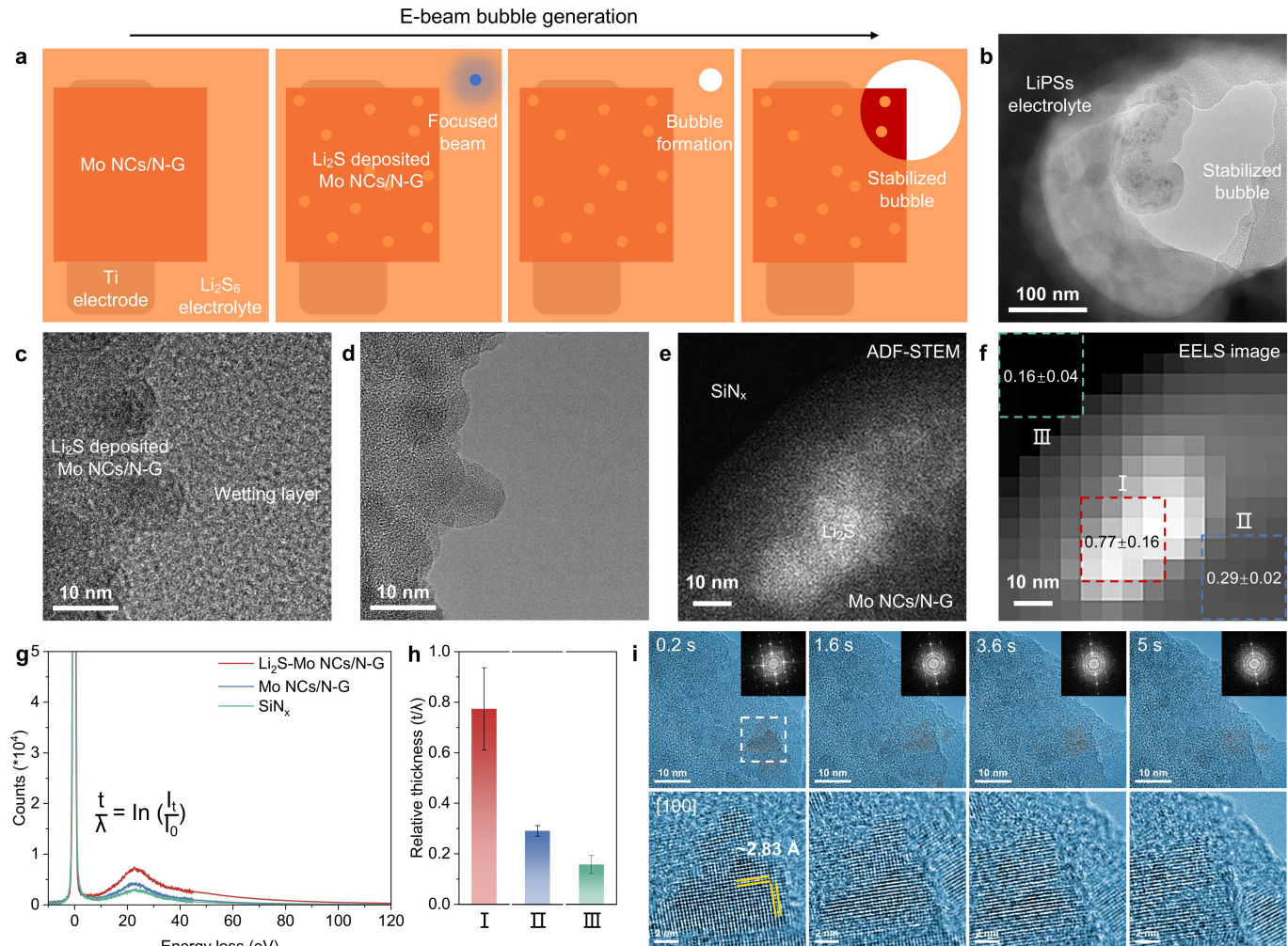
Extended Data Fig. 3 | Interfacial reactions of LiPSs at -0.1 V without mediation of active centres. **a**, Comparison of output current during potentiostatic discharge at -0.1 and -0.5 V in electrochemical liquid cells. The current density was reduced by half at -0.1 V . **b**, The projection-area variation as a function of time of particles #5 and #6. Error bars represent standard deviations of the measurement. **c**, Time-series TEM images from Supplementary

Video 3 showing two-step Li_2S deposition in an electrochemical liquid cell during potentiostatic discharge at -0.1 V . $10\text{ mM Li}_2\text{S}_6$ was used as the electrolyte. **d**, Statistics of rod and particle quantity at specific times corresponding to the dashed white frame area in the TEM image (0.6 s). **e**, Time-series TEM images of typical two-step deposition of Li_2S by means of metastable Li_2S_2 (marked by dotted white lines). TEM images of I-IV correspond to the typical areas at 72.6 s.



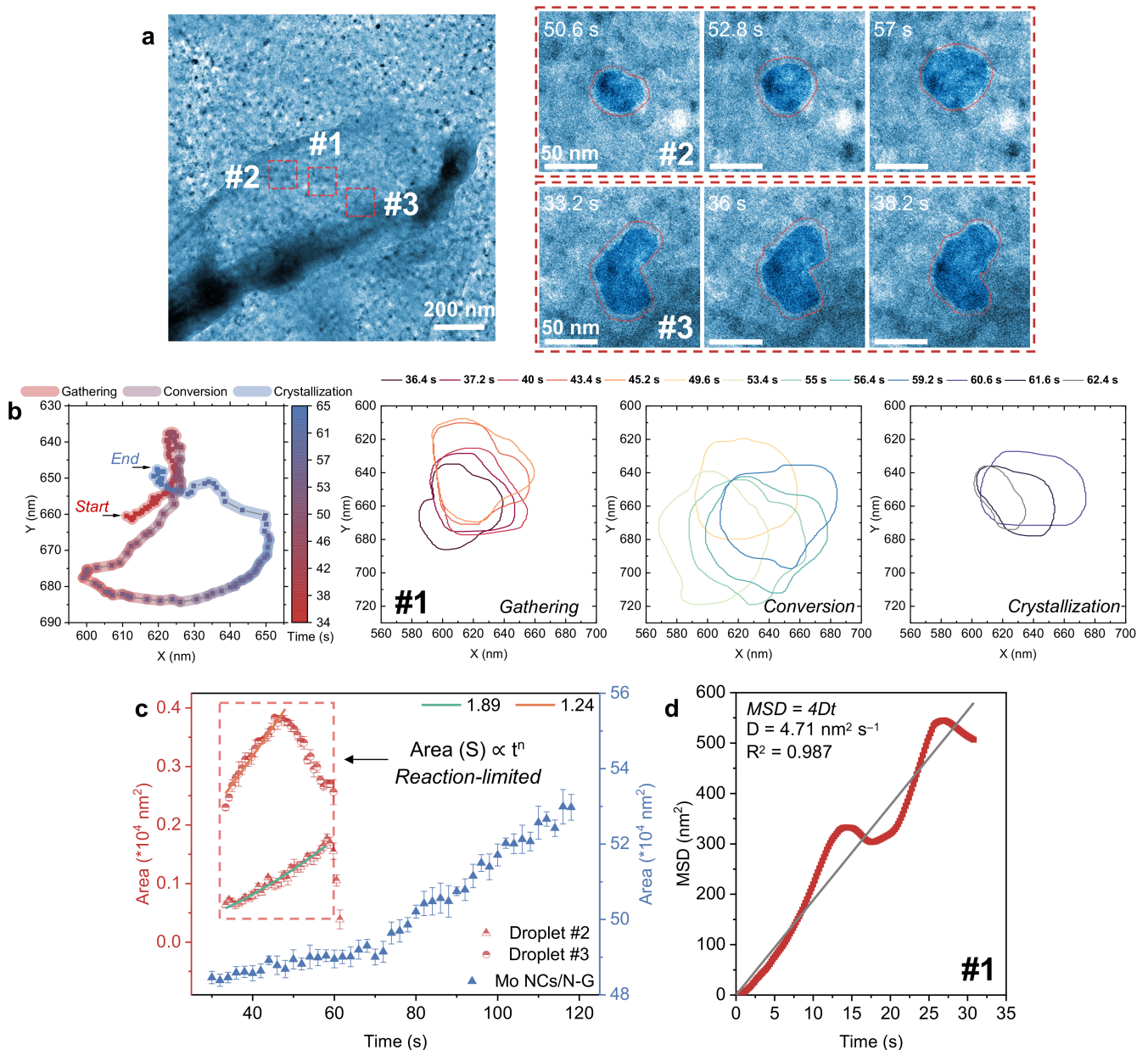
Extended Data Fig. 4 | In situ EC-TEM studies of Li_2S deposition with mediation of active centres. **a**, The projection-area variation as a function of time of Mo NCs/N-G and time-series TEM images from Supplementary Video 4. The electrochemical liquid cell was potentiostatically discharged at -0.5 V using $10\text{ mM Li}_2\text{S}_6$ as the electrolyte. Error bars represent standard deviations of the measurement. **b**, Time-series TEM images to further observe the dashed red square area of Extended Data Fig. 4a (185 s) under a higher magnification (Supplementary Video 5). The electrochemical liquid cell was further potentiostatically discharged at -0.5 V . Many dark areas (marked with dotted

red circles) and deposited particles (marked with white arrows) were observed. **c**, Time-series TEM images from Supplementary Video 6. The electrochemical liquid cell was potentiostatically discharged at -0.5 V using $100\text{ mM Li}_2\text{S}_6$ as electrolyte. The imaging area was divided into electron-inaccessible/accessible areas. Li_2S deposition mainly proceeded on electron-accessible areas of Mo NCs/N-G, whereas no change was observed on the electron-inaccessible area and bare Ti electrode surface. This indicated the high reaction activity of Mo NCs/N-G for electrochemical deposition of Li_2S .



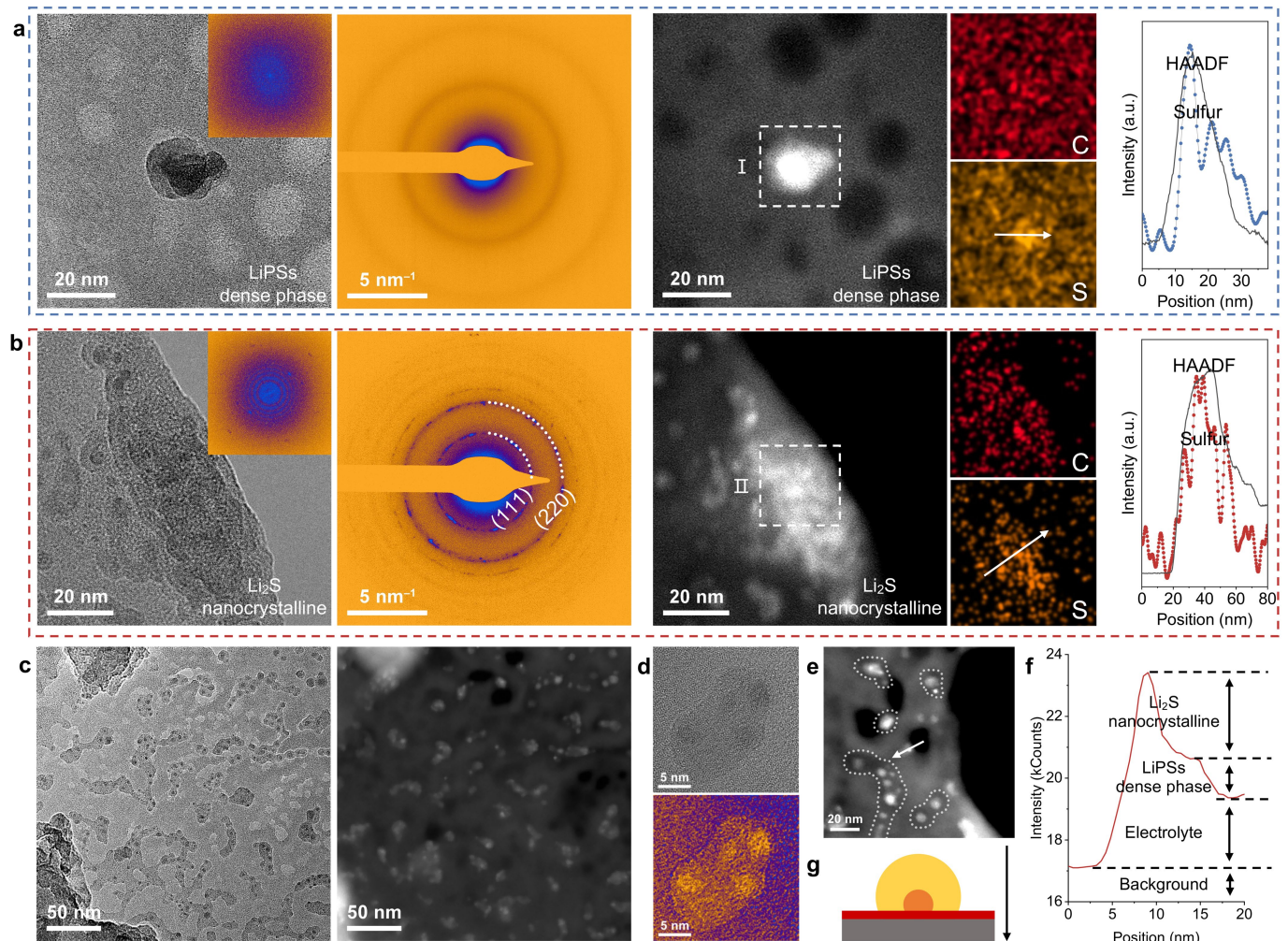
Extended Data Fig. 5 | Method of HRTEM observation in an electrochemical liquid cell. **a**, Schematic illustration of the ‘e-beam bubble generation’ method for HRTEM observation of Li₂S nanocrystalline deposited on Mo NCs/N-G nanosheet. Following the electrochemical deposition of Li₂S through a potentiostatic discharge at −0.5 V, the e-beam was focused on the bulk electrolyte for the generation of bubbles. Once the bubble area stabilized, the atomic structure of Li₂S nanocrystalline can be obtained, with the image resolution being mainly determined by the thickness of SiN_x layers. **b**, TEM images showing different areas of the LiPSS electrolyte, Li₂S nanocrystalline deposited on Mo NCs/N-G and the stabilized bubble area. **c,d**, HRTEM images

before and after the removal of the wetting layer of electrolyte. **e,f**, Annular dark-field scanning TEM (ADF-STEM) image and the corresponding EELS image for relative thickness measurement in liquid cells. **g**, Typical low-loss EELS of Li₂S nanocrystalline (I), Mo NC/N-G nanosheets (II) and SiN_x layers (III) as marked in the EELS image. **h**, Average relative thickness obtained by the log ratio method in Digital Micrograph software. Error bars represent standard deviations from several EELS curves. **i**, Time-series HRTEM images, corresponding FFT patterns and partial enlarged details of Li₂S nanocrystalline deposited on Mo NCs/N-G obtained in an electrochemical liquid cell.



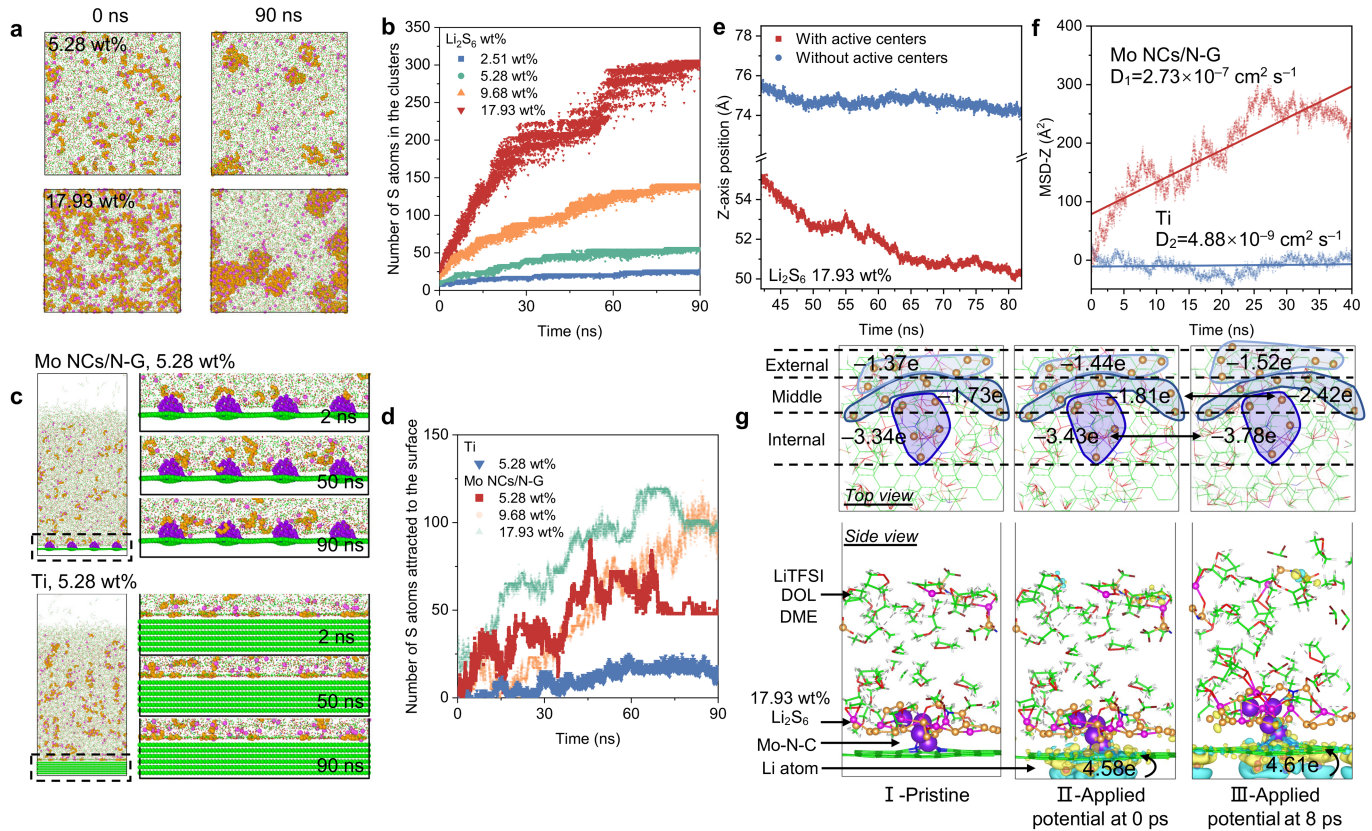
Extended Data Fig. 6 | Analysis of in situ EC-TEM studies of redox reactions of LiPSs with mediation of active centres. **a**, Time-series TEM images from Supplementary Video 7 showing several droplets in different areas (highlighted in red). **b**, Motion trajectory of the mass centre of droplet #1 and the corresponding edge contour plots of droplet #1 in Fig. 4b. It included the typical processes of gathering, conversion and crystallization. **c**, Projection-area variation of droplets #2 and #3 (red) and Mo NCs/N-G (blue) as a function of time during potentiostatic discharge. A power function was used to fit the area variation of droplets #2 and #3 over time (area $\propto t^n$) according to the

Lifshitz–Slyozov–Wagner model, in which $n \geq 1$ represents reaction-limited growth. After a rapid decrease in the size of droplets of LiPSs, there was an obvious increase in the projection area of Mo NCs/N-G nanosheet, similar to that in Extended Data Fig. 4a,b, which should be attributed to the deposition of Li₂S. Error bars represent standard deviations of the measurement. **d**, MSD analysis of droplet #1 as a function of time. The two-dimensional diffusion coefficient (D) was calculated to be $4.71 \text{ nm}^2 \text{ s}^{-1}$. The initial point of MSD corresponds to 34.4 s of droplet #1 in Fig. 4b.



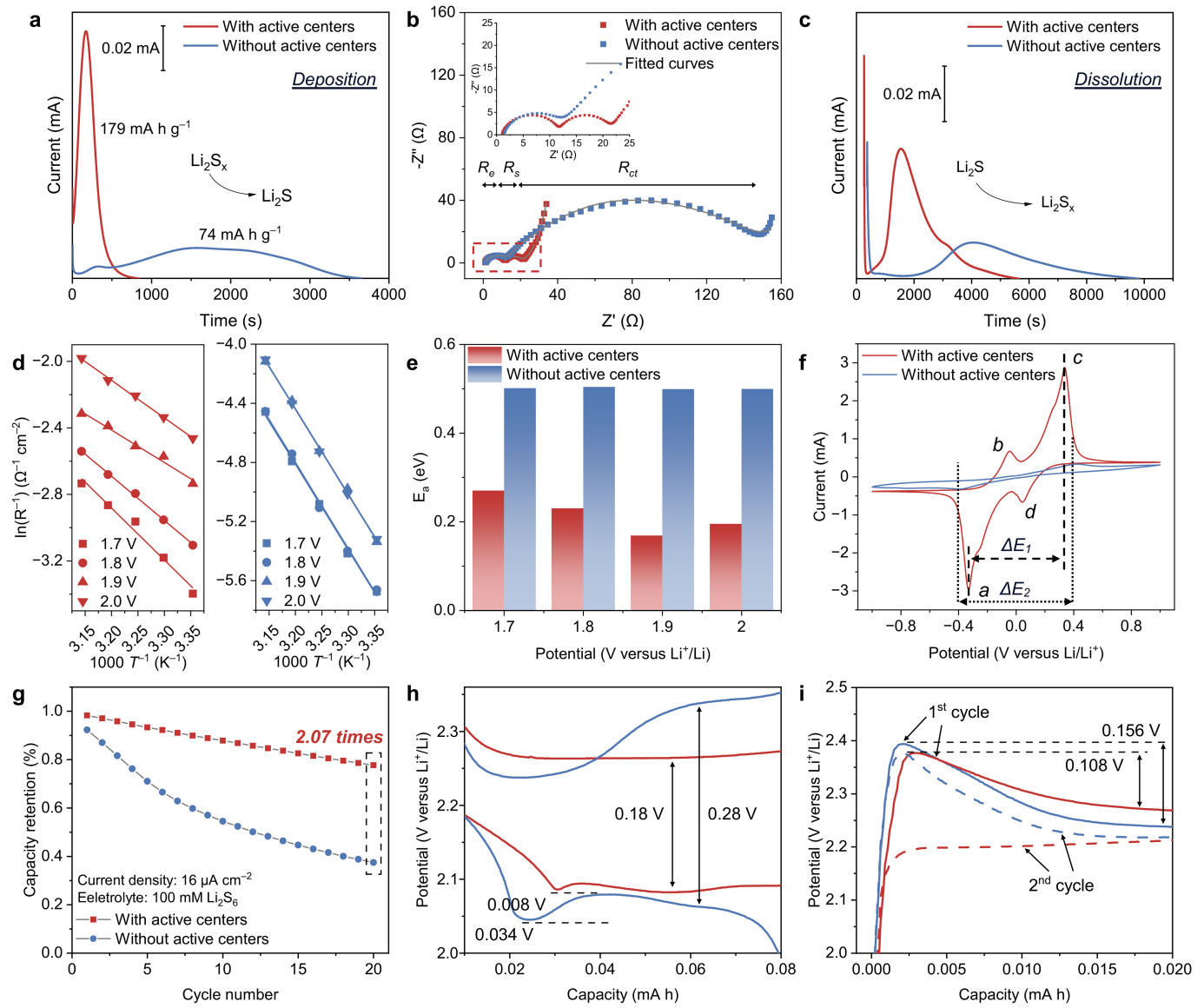
Extended Data Fig. 7 | Structure characterization of droplet-like dense phase. **a,b**, Comparative characterization of the dense phase of LiPSs and Li₂S nanocrystalline, including HRTEM images, the corresponding FFT and SAED patterns, HAADF-STEM images, EDS mappings and the corresponding linear elemental analysis. **c**, TEM and HAADF-STEM images of Mo NCs/N-G nanosheet after the electrochemical deposition in a liquid cell, showing the dense phase of LiPSs and Li₂S nanocrystalline from a wider observation region. **d**, Raw and post-processed HRTEM images using a Gaussian filter. To solve the scattering and artefacts in HRTEM images resulting from amorphous SiN_x windows,

disordered electrolyte and the contrast transfer function of the electron microscope, a Gaussian filter was applied to suppress high-spatial-frequency noise and enhance the boundary of dense phase areas. **e,f**, Partial enlarged details of the HAADF-STEM image and the corresponding linear HAADF intensity analysis. The areas of the dense phase of LiPSs are marked by the dotted white lines. The linear HAADF intensity analysis is marked by the white arrow. The contrast contribution of HAADF intensity can be attributed to Li₂S nanocrystalline, dense phase of LiPSs, electrolyte and background, respectively. **g**, Schematic illustration of the path of scattered electrons.



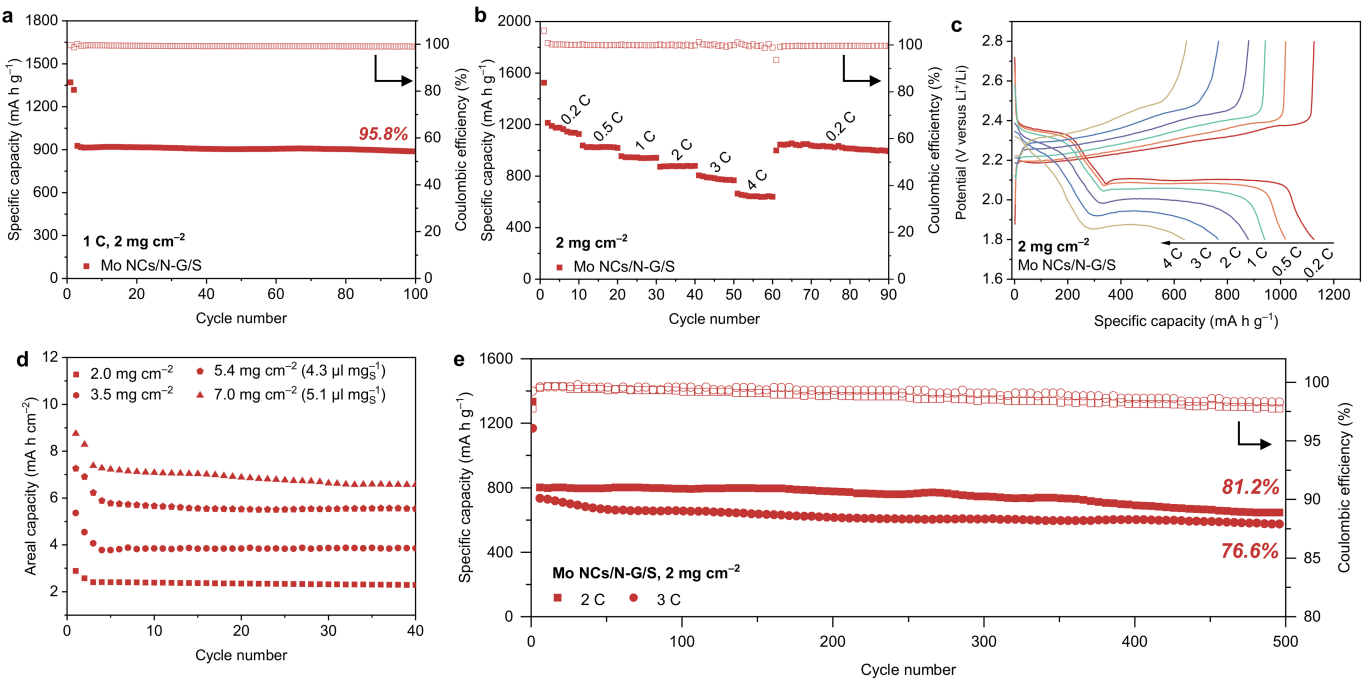
Extended Data Fig. 8 | MD simulations and DFT calculations at different interfaces. **a**, Snapshots of MD simulations with different Li_2S_6 concentrations of 5.28 wt% and 17.93 wt%. **b**, Statistics of S atoms in aggregated clusters with different electrolyte concentration. The five largest clusters were used to calculate the average number of contained S atoms. **c**, Snapshots of MD simulations on different surfaces of Mo NCs/N-G and Ti with Li_2S_6 concentration of 5.28 wt%. The right row is the enlarged view of the interface details and the initial S_6^{2-} and Li^+ ions were randomly dispersed in the electrolyte. After the NVT relaxation of 2 ns, the sampling results indicate that Mo NCs/N-G had a strong long-range attraction with S_6^{2-} ions. **d**, Statistics of S atoms attracted to the electrode surfaces of Mo NCs/N-G and Ti with different electrolyte concentration. **e**, Comparison of z-axis position variation (\AA) of dense ion-complex phase at different interfaces as a function of time corresponding to MD simulations in Fig. 4e with Li_2S_6 concentration of 17.93 wt%. The z-axis

distance is defined from droplets of LiPSs to the electrode surfaces (Ti or Mo NCs/N-G). **f**, MSD analysis of Li_2S_6 movement along the z-axis direction. The diffusion coefficients of S atoms in Li_2S_6 molecules over Mo NCs/N-G (D_1) and Ti (D_2) surfaces were $2.73 \times 10^{-7} \text{ cm}^2 \text{ s}^{-1}$ and $4.88 \times 10^{-9} \text{ cm}^2 \text{ s}^{-1}$, respectively. The initial point of MSD corresponds to 42 ns of the simulation. **g**, AIMD simulation of charge variation of polysulfide ions around Mo active centres from a top view and a side view. Considering the dynamic charge distribution, the polysulfide ions in the dense phase are defined as S_6^- ions in AIMD simulations. S_6^- ions in the dense phase are divided into internal, middle and external layers according to the distances from Mo active centres when viewed from the top. The charge-distribution diagrams, shown from left to right, include pristine structure relaxed for 20 ps before applying the electrode potential (I) and simulations at 0 ps (II) and 8 ps (III) after applying the electrode potential.



Extended Data Fig. 9 | Evaluation of electrochemical behaviour using Li_2S_6 electrolyte (100 mM) in coin-type cells. **a**, Potentiostatic discharge profiles of Li_2S deposition at 2.05 V with/without active centres. The scale of the yaxis is indicated by the bar. **b**, Nyquist profiles of EIS after potentiostatic discharge. R_e , R_s and R_{ct} indicate the resistance of electrolyte, surface layer and charge transfer, respectively. The inset is the local magnification profiles. **c**, Potentiostatic charge profiles of Li_2S dissolution at 2.4 V with/without active centres. The scale of the yaxis is indicated by the bar. **d**, Arrhenius plots of the linear relationship between logarithmic values of the reciprocal of R_{ct} and

the reciprocal of absolute temperatures for 1.7, 1.8, 1.9 and 2.0 V, with (red)/without (blue) active centres. **e**, Comparison of the corresponding E_a calculated on the basis of the slope of linear fitting. The E_a values with/without active centres are 0.27/0.5, 0.23/0.5, 0.17/0.49 and 0.19/0.49 eV, corresponding to the discharge potentials of 2.0, 1.9, 1.8 and 1.7 V, respectively. **f**, CV profiles of symmetric cells with/without active centres at a scan rate of 0.1 mV s^{-1} . **g**, Comparison of cycling performance with/without mediation of active centres at $16 \mu\text{A cm}^{-2}$. **h,i**, Corresponding charge/discharge profiles at specific cycles, showing the energy barriers of Li_2S nucleation and dissolution.



Extended Data Fig. 10 | Evaluation of electrochemical performance in Li–S batteries. **a,b**, Cycling performance (1C, 100 cycles) and rate performance (0.2, 0.5, 1, 2, 3, 4 and 0.2 C) of Mo NCs/N-G/S, with the sulfur areal loading of 2 mg cm^{-2} . A battery activation was performed at 0.2 C for two cycles (cycling performance) and 0.1 C for one cycle (rate performance), respectively. **c**, Charge/discharge profiles from rate performance of Mo NCs/N-G/S at 0.2, 0.5, 1, 2, 3

and 4 C. **d**, Cycling performance of Mo NCs/N-G/S at 0.2 C for 40 cycles with different sulfur areal loading of 2, 3.5, 5.4 and 7 mg cm^{-2} . A battery activation was performed at 0.05 C for two cycles. **e**, Long-term and high-rate cycling performance at 2 and 3 C for 500 cycles. A battery activation was performed at 0.2 C for two cycles. The capacity value is selected every five cycles.